SYNTHESIS, PROPERTIES AND APPLICATIONS OF TUNGSTEN OXIDE NANOSTRUCTURES

A Thesis Submitted to
the Graduate School of Engineering and Sciences of
İzmir Institute of Technology
in Partial Fulfillment of the Requirements for the Degree of

DOCTOR OF PHILOSOPHY

in Photonics Science and Engineering

by
Zeynep KAHRAMAN

December 2023

İZMİR

We approve the thesis of **Zeynep KAHRAMAN**

Examining Committee Members:

Prof. Sinan Balcı
Department of Photonics, IYTE

Prof. Mustafa Emrullahoğlu
Department of Photonics, IYTE

Assoc. Prof. Dr. Engin Karabudak
Department of Chemistry, IYTE

Dr. Öğr. Üyesi Murat Alkan
Department of Metallurgy and Materials Engineering, DEU

Assoc. Prof. Dr. Muhammed Üçüncü
Department of Pharmacy, İKÇU

11 December 2023

Prof. Sinan Balcı
Supervisor, Department of Photonics
IYTE

Assoc. Prof. Dr. Aziz Genç
Co-Supervisor, Department of Materials Science and Engineering
IYTE

Prof. Dr. Canan Varlıklı
Head of the Department of Photonics

Prof. Dr. Mehtap EANES
Dean of the Graduate School of Engineering and Sciences

ACKNOWLEDGMENTS

First of all, I would like to thank my thesis advisor, Assoc. Prof. Dr.Aziz Genç, who directed my interest throughout this thesis and transferred his knowledge in a very selfless way. He has created a good role model for me not only with his academic identity and success, but also with his ethical and human values, and I hope I will be an academician like him in the future.

Afterwards, I would like to thank my other advisor, Prof. Dr. Sinan Balcı, for allowing me to use the laboratory facilities very comfortably and for his very constructive attitude throughout my thesis work. I would like to thank my valuable jury members for their time and contributions to the development of my work and thesis.

To my dear friends especially Ayhan Tertemiz, Metin Tan, Cansu Kul, Tuğçe Arica Güvenç, Meriç Güvenç, Helin Yıldırım Özcan, Mehmet Özcan, Mine Nohuz, who never hesitate to share their friendship, their help whenever I need it, their time, who allow me to spend a unique time sometimes in academic life and sometimes in social life, and for their contribution to me in overcoming every problem during this time; I would like to thank everyone.

ABSTRACT

SYNTHESIS, PROPERTIES AND APPLICATIONS OF TUNGSTEN OXIDE NANOSTRUCTURES

In this study, tungsten oxide nanostructures, which are n-type semiconductors with a band gap between 2.6-2.8 eV, have been studied extensively. The hydrothermal method was used as the synthesis technique and the phases and morphologies were optimized in a stable and controllable manner. Firstly, stoichiometric tungsten oxide nanowires with certain ratios were synthesized, and then cobalt doping was made using this synthesis technique. Subsequently, sub-stoichiometric tungsten oxide nanowires, which have oxygen gaps and can show plasmonic properties due to the increased carrier density, were synthesized, and tungsten oxides with a flower-like hierarchical structure with oxygen gaps were synthesized and grouped according to possible application areas.

Accordingly, how oxygen vacancies and hierarchical structures affect photocatalysis applications have been examined and it has been seen that sub-stoichiometric tungsten oxide works faster until it reaches a certain saturation than stoichiometric tungsten oxide. According to this study, how the system can be manipulated by adding reducing pH to the system and hydrogen peroxide as an electron acceptor, respectively. It has been observed that it can be done.

Hierarchical tunsten oxide has been found to be an ideal catalyst that can work quickly in photocatalysis studies due to its hierarchical structure, which has oxygen vacancies and can absorb light well.

Additionally, tungsten oxide attracts attention as a material used in supercapacitor applications. Supercapacitors are long-lasting and fast-reacting electrochemical devices that can provide high power in energy storage and discharge processes. The use of tungsten oxide in supercapacitor applications can be summarized as follows: when nanoparticles with large surface area are used as electrode material, they increase the interaction with the electrochemical surface and can increase the energy storage capacity. It shows high electrochemical activity as an electrode material. This feature contributes to the high performance of the supercapacitor. Tungsten oxide has a structure suitable for electron and ion conduction. This allows the supercapacitor to have fast charge/discharge capabilities and low internal resistance. Tungsten oxide can show stable performance

during electrochemical cycles. This feature ensures the long life of the supercapacitor. In supercapacitor applications, in addition to these features, the electrical conductivity of the material can be increased by increasing the number of electrons carried in the material due to its oxygen gap. Accordingly, we investigated the comparative electrochemical properties and cycling stability of stoichiometric and sub-stoichiometric nanowires. Thanks to its electrochromic properties, the latest application has observed electrochromic changes of oxygen vacancies and cobalt doping.

ÖZET

TUNGSTEN OKSİT NANOYAPILARIN SENTEZİ, ÖZELLİKLERİ VE UYGULAMALARI

Bu çalışmada n tipi ve 2.6-2.8 eV arası bant aralığına sahip yarı iletken olan tungsten oksit nanoyapılar geniş kapsamda çalışılmıştır. sentez tekniği olarak hidrotermal yöntem kullanılmış olup fazları ve morfolojileri karalı bir şekilde kontrol edilebilir şekilde optimizeleri yapılmıştır. öncelikle belirli oranlara sahip stokiometrik tungsten oksit nanoçubuklar sentezlenmiştir sonrasında bu sentez tekniğinden yararlanıp kobalt katkılama yapılmıştır. Daha sonrasında oksijen boşluklarına sahip olan ve bu özelliklerinden dolayı plazmonik özellik gösterebilen stokiometri altı tungsten oksit nano çubuklar sentezlenmiş olup yine oksijen boşluklarına sahip çiçek benzeri hiyerarşik yapıya sahip tungsten oksitler sentezlenmiş olup olası uygulama alanlarına göre gruplandırılıştır.

Buna göre oksijen boşluklarının ve hiyerarşik yapıların fotokataliz uygulamalarını nasıl etkilediği incelenmiş ve görülmüştür ki stokiometri altı tungsten oksitin stokiometrik tungsten oksite göre belirli bir doygunluğa ulaşana kadar daha hızlı çalışmıştır, bu çalışmaya göre sisteme sırasıyla düşük ph, sisteme elektron alıcısı olarak hidrojen peroksit eklenerek sistemin nasıl manipüle edilebileceği izlenmiştir.

Hiyerarşik yapılı tunsten oksit ise hem oksijen boşluklarına sahip olması hemde ışığı iyi absorbe edebilen hiyerarşik yapıısndan dolayı fotokataliz çalışmalarında hızlı çalışabilen ideal bir katalizör olduğu görülmüştür.

Ayrıca tungsten oksit, süperkapasitör uygulamalarında kullanılan bir malzeme olarak dikkat çeker. Süperkapasitörler, enerji depolama ve deşarj süreçlerinde yüksek güç sağlayabilen, uzun ömürlü ve hızlı tepki veren elektrokimyasal cihazlardır. Tungsten oksitin süperkapasitör uygulamalarındaki kullanımı şu şekillerde özetlenebilir: geniş yüzey alanına sahip nanoparçacıklar elektrot malzemesi olarak kullanıldığında elektrokimyasal yüzey ile etkileşimi artırır ve enerji depolama kapasitesini artırabilir. elektrot malzemesi olarak yüksek elektrokimyasal aktivite gösterir. Bu özellik, süperkapasitörün yüksek performans sergilemesine katkıda bulunur. Tungsten oksit, elektron ve iyon iletimi için uygun bir yapıya sahiptir. Bu, süperkapasitörün hızlı şarj/deşarj yeteneklerine ve düşük iç dirence sahip olmasına olanak tanır. Tungsten oksit,

elektrokimyasal döngüler sırasında kararlı bir performans gösterebilir. Bu özellik, süperkapasitörün uzun ömürlü olmasını sağlar. Süperkapasitör uygulamalarında bu özelliklerinin yanı sıra oksijen boşluğuna sahip olması malzemenin içinde taşınan elektron sayısı artarak malzemenin elektrik iletkenliği arttırılabilir. Buna göre stokiometrik ve stokiometri altı nanoçubuklarının karşılaştırmalı olarak elektrokimyasal özellikleri ve döngü tekrarlama konusundaki stabiletelerini araştırdık. Kendi bünyesinde taşıdığı elektrokromik özellikleri sayesinde en son uygulama olarak oksijen boşluklarının ve kobalt katkılamanın elektrokromik olarak değişimleri gözlenmiştir.

Dedicated to all people who are sensitive to animals and the environment...

TABLE OF CONTENTS

LIST OF FIGURES

CHAPTER 1

INTRODUCTION

Since transition metal oxides can be easily formed through self-assembly in various nanostructures such as nanowires, nanotubes, nanoribbons, nanosheets, and because these various structures can show different and unique optical, electronic, magnetic and physical properties according to their surface, confinement effects, width areas and aspect ratios[1,2]. The fact that transition metal oxides have a d-orbital gives the materials unique properties such as wide band gaps, optical and electrical properties, high dielectric constant, and superconductivity with their strong electron correlation effect (coulomb interaction)[3-8]. This easily expands the range of different usage areas and they have begun to attract a lot of attention in terms of their use in different technological fields[9,10]. However, as metal oxides have become widespread due to their non-toxicity and high thermal and chemical stability, these materials are effectively used in energy storage systems such as smart window systems, supercapacitors, as well as in optical and electronic device applications such as light emitting diodes, sensors, photocatalysis, solar cells and photodetectors[11-19]. The fact that metal oxides form oxygen vacancies and show plasmon absorption in the visible and near-infrared regions shows that studies on Localize Surface Plasmon Resonance (LSPR) should not be limited to metals only[20,116].

Among metal oxides, tungsten oxide (stoichiometric WO_3 and non-stoichiometric WO_{3-X} with oxygen vacancies) is becoming the focus of attention due to its physical and chemical properties. Photocatalysis reactions, in which metal oxides can change the speed of chemical reactions when exposed to light, have been realized mostly by working with TiO_2, thanks to Honda's groundbreaking work[22-25]. However, since TiO_2 has a band gap of 3.2 eV, allowing it to be excited only in the UV region, sunlight cannot be used effectively for photocatalysis applications. However, tungsten oxide, an n-type semiconductor with a band gap of 2.6-2.8 eV, gives very good results in the infrared and visible regions, so it is transmitted from the sun to our world[26-29]. It enables you to benefit from the incoming light in the most efficient way.

Although the use of the sun, a renewable energy source, and the cleaning of pollutants from water through photocatalysis reactions using solar energy contribute

significantly to a clean future, we must emphasize that energy efficient storage systems should also be taken into consideration to the same extent. In this way, the importance of developing supercapacitors, known as efficient energy storage devices, is increasing[30,31]. Thus, with their environmental friendliness, fast charge-discharge features and high capacitance values, supercapacitors will be included in many application areas, including electric vehicles[32,33]. Although graphene with a high charge-discharge ratio is mostly used, its low volumetric capacitance has led to the search for new materials[34]. The main factors that determine the performance of supercapacitors are surface area and pore size distribution. While these tunable properties and the use of reversible faradic reactions to store energy make transition metal oxides important candidates for supercapacitors, especially the stable microstructure of tungsten oxide is an important advantage in terms of the continuity of reactions[35-37].

Electrochromism can be summarized as the temporary or permanent change of the optical properties of the material when a voltage is applied[38-40]. Electrochromic and photochromic devices can be shown as one of the important methods that can be a solution to the energy problem that continues to increase today in terms of energy efficiency and energy storage; It offers significant advantages in many areas such as energy saving, solar energy use and imaging technologies[41-43]. The first EC device was demonstrated by Deb in 1969 to show reversible color change of tungsten oxide[44]. From now on, many EC materials such as metal oxides, and conjugated polymers that will have electrochromic properties have been studied[45,46]. Thanks to the oxygen vacancies that can be found in the structures of metal oxides or their easy doping with metal, the efficiency and speed of the devices are increased and thus the performance of the devices can be modulated[47-50]. There are 5 layers in the structure of a classical electrochromic device: conductive electrodes on both surfaces, ion storage layer, electrolyte and electrochromic material[51,53]. The use of many different electrolytes (including Li^+, Na^+, K^+, Mg^{+2}, Ca^{+2}, Al^{+2}, Zn^{+2}, H^+) has been investigated, and we show here that liquid crystal with tungsten oxide is an effective electrochromic device[54,56].

Within the scope of this thesis, using the hydrothermal method, stoichiometric tungtsen oxide nanowire (WO_3), sub-stoichiometric tungsten oxide nanowire with oxygen vacancies that can show plasmonic properties (WO_{3-x}), flower-like tungsten oxide nanostructure with hierarchical structure (WO_{3-x}) and cobalt doped tungsten oxide ($CoWO_{3-x}$) were synthesized. The experimental method is detailed in Chapter 1. Chapter 2 includes SEM and XRD results for microstructure characterization. The definition of photocal-

ysis and detailed explanation of its application areas and the performances of tungsten oxide in photocatalysis applications are included in Chapter 3. In particular, it is examined how its oxygen vacancies and hierarchical structures affect photocatalysis reactions. The experimentally found absorption graphs are also found theoretically with the help of FDTD simulation, and thus the optical characterization measurements of tungsten oxide nanowires , such as refractive index and dielectric coefficients, are included in Chapter 4. Chapter 5 covers the performances and electrochemical characterizations of substoichiometric and stoichiometric nanowires with oxygen vacancy for supercapacitor applications. Finally, in Chapter 6, the first thing that comes to mind when electrochromic is mentioned is the electrochromic applications of tungsten oxide. Liquid crystal was used as the electrolyte for these applications, and it was examined how the structure being stoichiometric, having oxygen vacancies, and metal doping changed the device performances

CHAPTER 2

SYNTHESIS TECHNIQUES

All syntheses were performed using the hydrothermal method. Hydrothermal is actually a term of geological origin that means the crystallization of minerals depending on their solubility under high temperature and high vapor pressure. It is a method of synthesizing nanoparticles under high pressure and high temperature in an oven (reaction temperatures < 300 °C) by placing a teflon-lined container in which the precursor material is placed along with a solvent, in a steel pressure container called an autoclave (Fig.2.1)[57]. The method has advantages such as being easy, environmentally friendly, homogeneous distribution in solution, and inexpensive.

2.1 Synthesis of Stoichiometric Tungsten Oxide Nanowires

For the synthesis WO_3 nanowires, first, 5 mmol of sodium tungstate was dissolved in 50 ml of distilled water, then HCl was added dropwise so that the pH of the product was approximately 1.5. To this slightly yellow colored tungstenic acid solution, 5 mmol Na_2SO_4 was added to produce WO_3 nanowires was mixed separately for about half an hour at room temperature. The resulting solution was placed in teflon-lined, stainless steel autoclaves, left for 12 hours in the oven at 180 degrees, and then cooled at room temperature, then cetrifuged by washing with ethanol and water in order to remove supernatants and remaining precursor. The gray-white samples obtained were left under vacuum in an oven at 60 degrees overnight to dry.

2.2 Synthesis of Sub-Stoichiometric Tungsten Oxide Nanowires

In fact, it is quite similar to stoichiometric tungsten oxide as a synthesis technique. 5 mmol sodium tungstate was added to 50 ml of distilled water and placed in a magnetic stirrer. HCl was added drop by drop and when the pH was approximately 1.5.

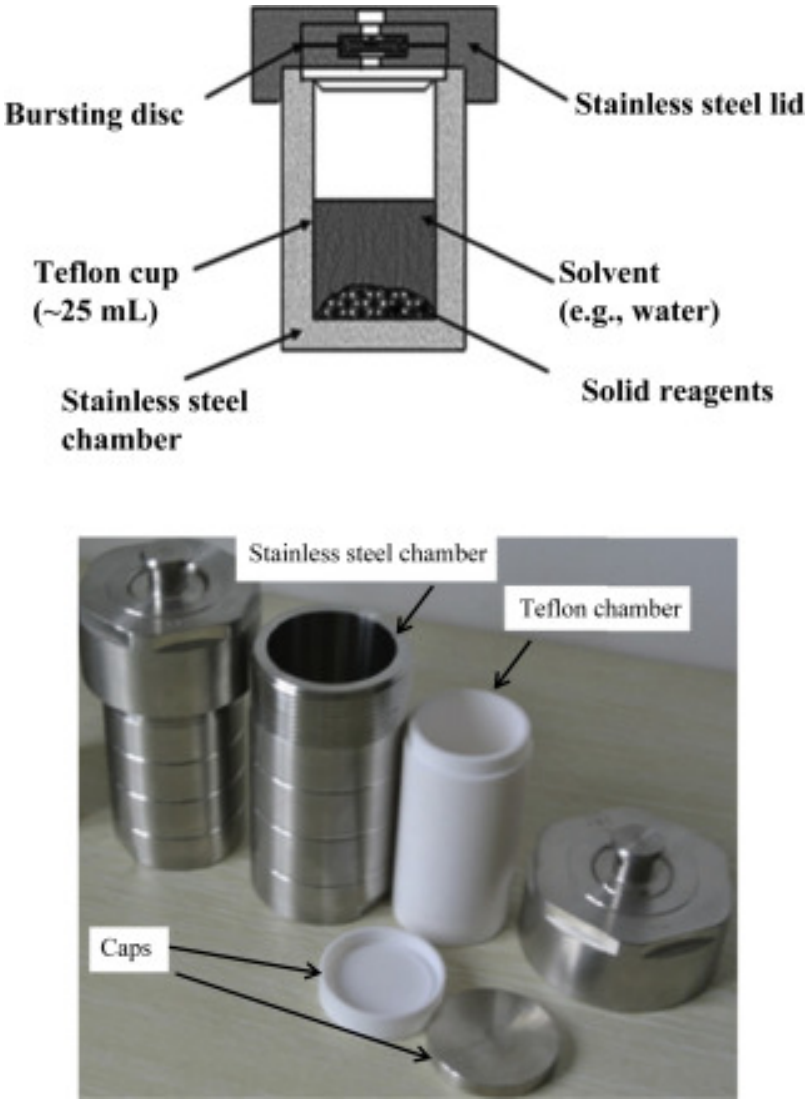

Figure 2.1. The main components of hydrothermal synthesis are the teflon-lined container placed in the autoclave and the solvent and precursor required for the experiment.

K_2SO_4 was added and left to mix at room temperature for half an hour. Then, the solution was placed teflon-lined in the autoclave and left in the oven at 180 degrees for 12 hours. The sample, which had a color between yellow and green, was washed several times with ethanol and water, then kept to dry in the vacuum oven at 60 degrees overnight.

2.3 Synthesis of Hierarchical Flower-like Sub-Stoichiometric Tungten Oxide

To synthesize hierarchical flower-like tungsten oxide with oxygen vacancies by the hydrothermal method, 2.52 mmol WCl_6 was added to 50 ml of ethanol as a solvent in a

beaker. After mixing in the magnetic stirrer for a while, the solution that turned blue was placed in Teflon containers. Then, the teflon containers were placed in autoclaves and kept in the oven at 180 degrees for 6 hours. After the temperature reached room conditions, it was washed with ethanol and water several times, respectively, using a centrifuge, and the resulting sample was left to dry under vacuum at 60 degrees overnight. The resulting powder turned into a green colored powder.

2.4 Synthesis of Co-Doped Tungsten Oxide Nanowires

By adding 5 mmol sodium tungstate, 5 mmol Na_2SO_4 and 1 mmol $CoCl_2$ into 40 ml of distilled water, the magnetic stirrer was mixed for 2 hours. The solution was placed in Teflon-lined containers and then placed in autoclaves and left in the oven at 180 degrees for 24 hours. After the temperature of the solution removed from the autoclaves reached room conditions, it was washed several times successively with ethanol and water, and a centrifuge was used for this washing each time. The resulting sample was left in a vacuum oven set at 70 degrees overnight to dry.

2.5 Synthesis of Flat-tipped and Sword-like Tungsten Oxide Nanowires

For flat-tipped tungsten oxide; after adding 5 mmol sodium tungstate into 50 ml of pure water, 950 μl of HCl was added drop by drop to bring the pH of the solution to approximately 1.5, then 8 mmol glycine and 0.1 g of sodium dodecyl sulfate (SDS) were added and placed in autoclaves with teflon containers in the oven at 180 degrees for 12 hours. It was kept waiting, washed with ethanol and water several times to remove the purified powders from the resulting solution, left in a vacuum oven at 60 degrees until it dried, and then kept at 300 degrees for 4 hours to anneal.

The synthesis of the sword-like structure is the same as the synthesis of the flat-tipped structure, the only difference is that SDS is not used in the sword-like structure and the synthesis method is exactly the same.

CHAPTER 3

CHARACTERIZATION METHODS

Nanostructured materials attract a lot of attention in new and rapidly developing fields such as optics, electronics, catalysis and energy storage. Nanostructured materials are called so because their size is in the nano range. It is very important to be able to determine the shape, size and crystal structure properties of these nanomaterials well in order to direct them to appropriate areas of use. The two most definitive methods for microstructure determination are scanning electron microscopy (SEM) for morphology and size determination, and X-ray diffraction method (XRD), which is the most effective method for determining crystal structure and phase.

3.1. Scanning electron microscopy (SEM)

Just as the optical microscope takes images using light, the electron microscope makes images using electrons. Since the wavelength of electrons is much smaller than the wavelength of light, its resolution is 1000 times clearer than optical microscopy. SEM-imaging system can therefore be considered as a standard for nanostructure characterization. The simple way the scanning electron microscope works is as follows, the electron gun at the top of the microscope produces electron beams[58]. Electrons following a vertical path in vacuum pass through electromagnetic fields and hit the sample in order to be directed towards the sample. Electrons and x-rays that hit the sample and scatter are collected with the help of detectors and converted into a signal to obtain the final image. The microstructure analysis of the as-prepared samples was examined using scanning electron microscopy (SEM) (FEI QUANTA 250 FEG). Fig. 3.2 a, 3.2 b and 3.2 c are the SEM image of sub-stoichiometric, stoichiometric nanowires and flower-like hierarchical structures. It is seen that sub-stoichiometric nanowires are very thin and long wires with a length of 5 μm and radius of 40 nm, stoichiometric nanowires is 210 nm and their length is mostly larger than 5 μm. Figure 3.3 shows tungsten oxide nanowires

with morphological differences. While tungsten oxides with flat-tipped are seen at 3.3 f, sword-like nanowire structures are seen at 3.3 f.

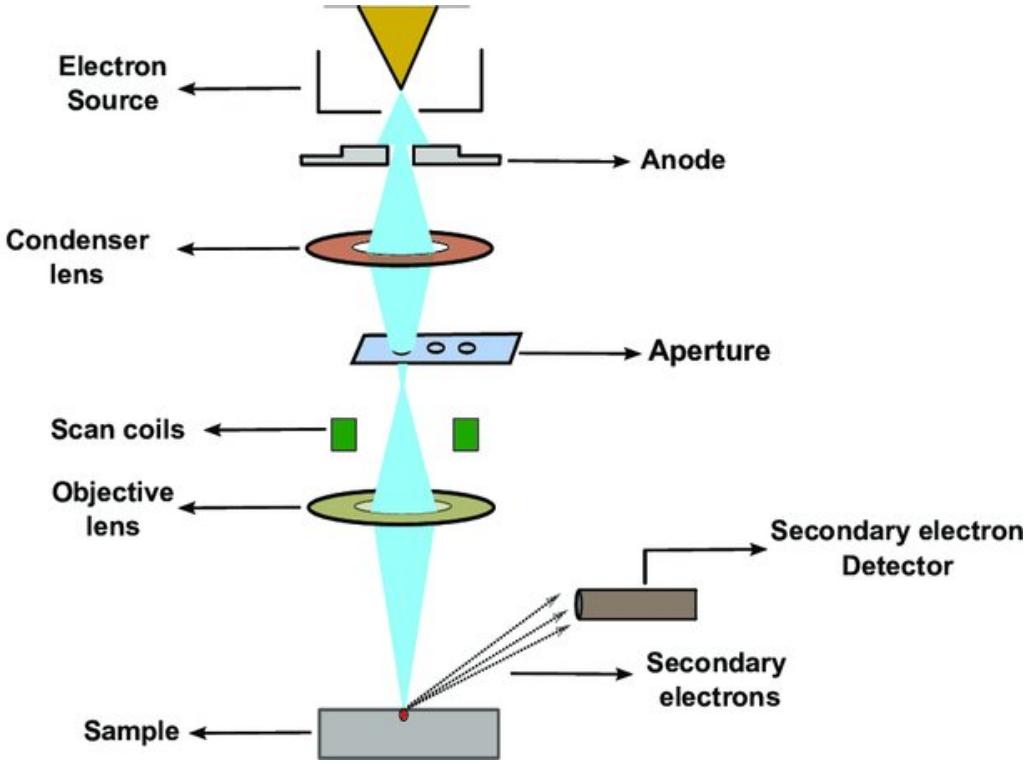

Figure 3.1. Working principle of SEM

3.2 X-ray diffraction (XRD)

X-ray diffraction (XRD), phase analysis, is the main method of crystallographic characterization for nano- and thin-film materials. The diffraction pattern of each structure is like the fingerprint of that structure, therefore it is one of the most powerful and fastest techniques for the determination of an unknown structure.

The following formula (3.1), known as Bragg diffraction, defines the working principle of XRD. According to this formula, it is related to the wavelength of the reflected X-ray (λ), the distance between atomic planes (d) and the diffraction angle (θ). When the x-ray encounters atoms inside the crystal, most of them will refract catastrophically; There will be x-ray interference in some directions. It behaves as if the X-rays were 'reflected' from a family of planes within the crystals (Fig 3.4).

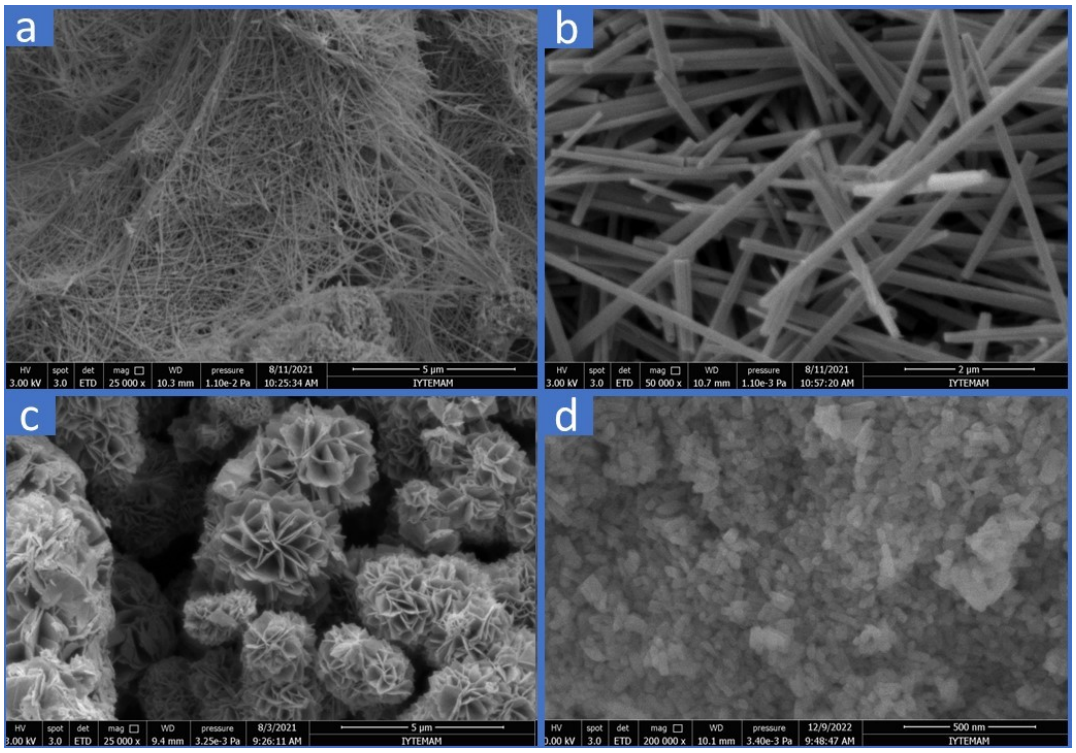

Figure 3.2. SEM images for morphology determination; a)sub-stoichiometric tungsten oxide with oxygen vacancies (WO_{3-x}), b)stoichiometric tungsten oxide (WO_3), c)flower-like tungsten oxide with hierarchical structure (WO_{3-x}), d) cobalt-doped tungsten oxide ($CoWO_4$).

$$n(\lambda) = 2d * sin\theta \tag{3.1}$$

Figure 3.5 a shows a typical XRD pattern of the stoichiometric tungsten oxide nanowires which can be indexed as hexagonal structure of WO_3 of unit cell with a= 7.32, b=7.32, and c=7.66 nm.

XRD pattern of sub-stoichiometric WO_{3-x} nanowires is shown Fig. 3.5 b. The diffraction peaks (2θ) are identified in relation to the monoclinic tungsten oxide phase. The lattice parameters of monoclinic tunsten oxide nanowires are as follows: a = 1.93, b = 3.78, and c = 17.07 nm. The peak at $2\theta = 23^0$ is characteristic of tungsten oxide (WO_{3-x}).

According to the XRD pattern of the hierarchical tungsten oxide structure, it is seen that it has an orthorhombic phase with lattice parameters a = 3.86, b = 18.42, c = 21.94 Å. It has characteristic peaks at 23, 25 and 34 degrees, corresponding to 2 θ (Figure 3.5 c)

The XRD pattern of cobalt doped tungsten oxide ($CoWO_4$) is shown in Figure 3.5 d. It is included in the monoclinic crystal structure system belonging to the 2/m space group, in accordance with the literature. The lattice parameters are as follows; a= 4.720,

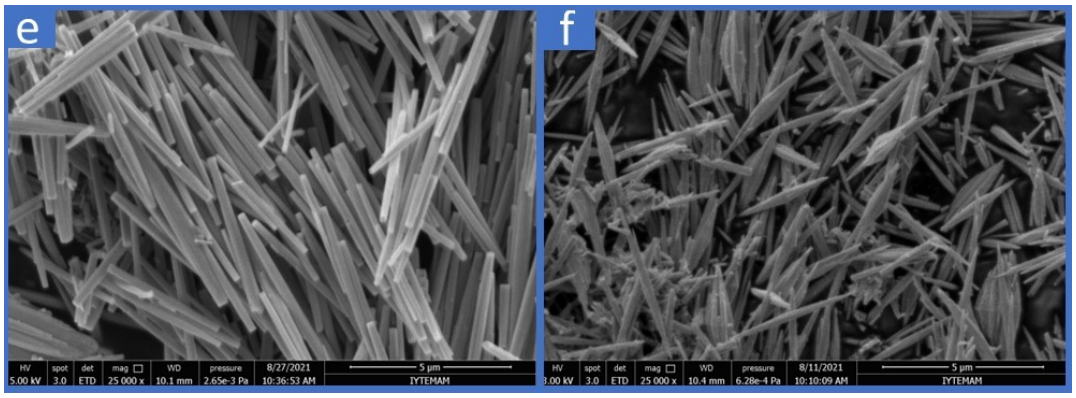

Figure 3.3. Sem images for morphology determination; e)flat-tipped tungsten oxide nanowires, f)sword-like tungsten oxide.

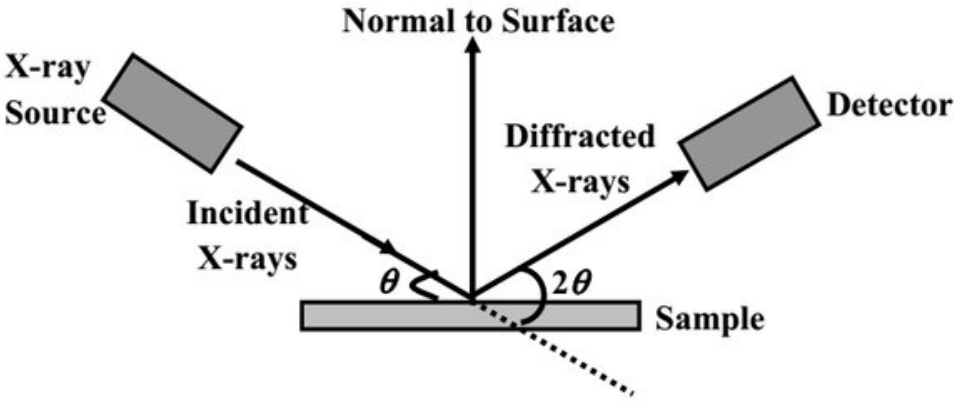

Figure 3.4. Schematic Representation on the Working Principles of X-ray Diffraction

b=5.06, c=5.67 Å. It has a characteristic peak at approximately 2θ = 30, however, it also has peaks at approximately 24, 23, 18 and 36 degrees, which are exactly compatible with the literature. Figure 3.6 shows the XRD results of sword-like and flat-tipped tungsten oxide nanorods. Considering the harmony in the graphs drawn on top of each other, it is clear that the phases of the two are the same and that they are similar to the XRD pattern of tungsten oxide nanowires in Figure 3.5 a and that they have a hexagonal structure.

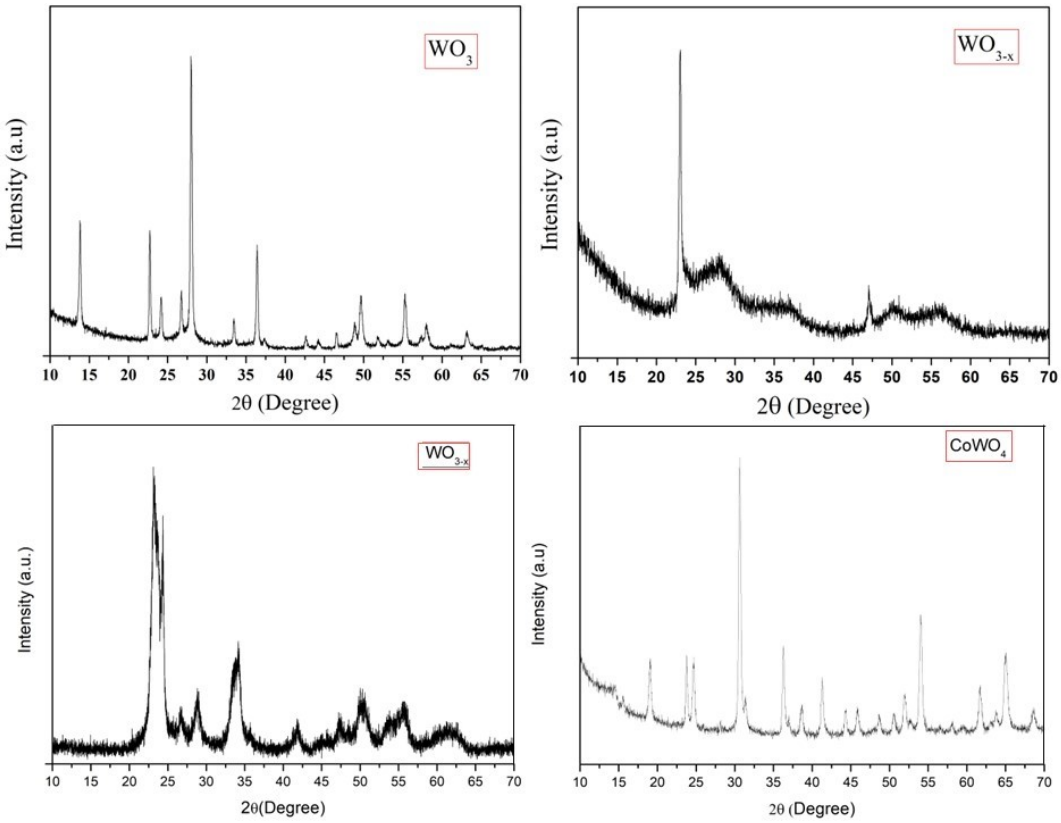

Figure 3.5. XRD images of tungsten oxide nanostructures.

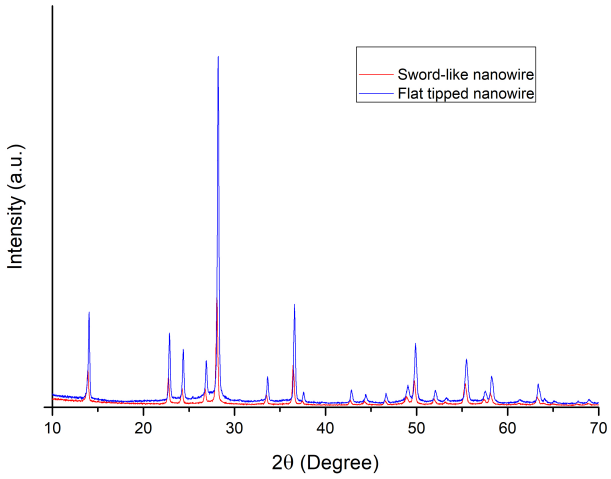

Figure 3.6. XRD images of tungsten oxide nanowires

CHAPTER 4

PLASMONIC METAL OXIDES

With the rapid development of nanotechnology and optics, new concepts aimed to include both fields have begun to be sought. Although it does not seem to be compatible with nanotechnology due to the diffraction limit of optics being a few hundred nanometers, the field of plasmonics, where metals create surface waves with the collective oscillations of conduction electrons, has become the focus of extreme interest[59,60]. Plasmonics has become a new concept that combines both important fields.

The fact that plasmonic materials have resonance modes that involve the interaction between free charges and light leads to the development of new device families such as optical nanoantennas, optical invisibility cloaks, surface enhanced Raman spectroscopy (SERS), light concentrators and superlenses with innovative and unprecedented functions that involve this light-matter interaction[61-65].

In calculating the plasma frequency, the Drude model explains the interaction of conduction electrons with the electromagnetic field by considering the conduction electrons as a three-dimensional free electron gas[66,67]. According to the Drude theory, the permeability of the material can be written as follows;

$$\varepsilon_m = 1 - \omega_p{}^2 / [\omega^2 + i\gamma\omega] \quad (4.1)$$

where the frequency dependent relative permittivity of the metal, ε_m, ω is the relaxation frequency associated with the metal, γ is the mean relaxation time of conduction electrons, and ω_p is the plasma frequnecy and the plasma frequency is given by equation 4.2.

$$\omega_p = [n * e^2]/[\varepsilon_0 * m] \quad (4.2)$$

Where n is the conduction electron density, e their charge, ε_0 is the relative permittivity of free space and the effective optical mass of conduction electrons is $m*$[68,69].

On the surface of a solid material such as a metal with a free charge, the surface charge (mostly electrons) oscillates collectively due to light irradiation. The electromagnetic wave strikes a metal at the plasma frequency and the surface plasmons are optically excited and light can be coupled to the surface plasmon modes propagating on the metal surface and the surface plasmons are excited. Thus, as seen in Fig. 4.1a

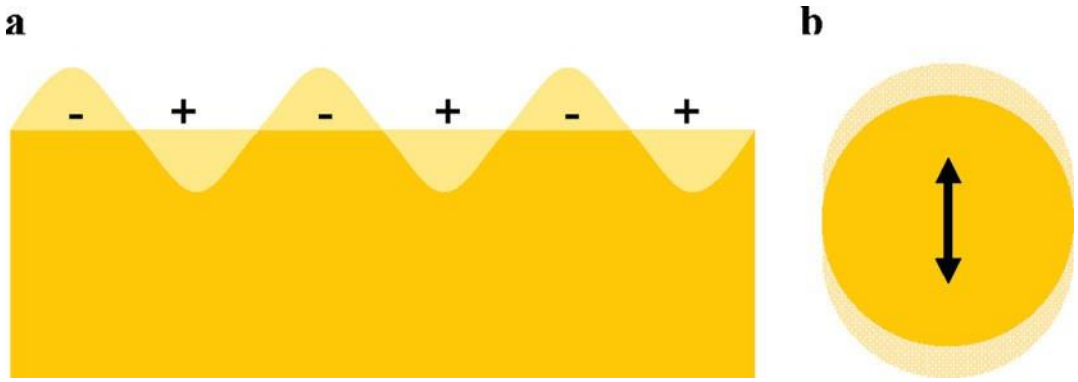

Figure 4.1. Illustrations of (a) surface plasmons and (b) a localized surface plasmon[65].

Another plasmonic effect is the localized surface plasmon (LSP). When confined to a particle, a nanoparticle, with a size comparable to the wavelength of light, as seen in Fig. 4.1b, the free electrons of the particle participate in collective oscillations.

Although the concept of plasmonics is identified with metals, localized surface plasmon resonances have been found to be a valid phenomenon in doped semiconductor nanocrystals, and localized surface plasmons, especially in the near-infrared region, have begun to be studied comprehensively[70-72]. The ability to adjust plasmonic properties by easily doping metal oxides or creating vacancies has emerged as an interesting field.

In metal oxide semiconductors, LSPRs can also be inherently tunable by varying the doping level and electrochemical potential; and allows the observation of plasmonic effects at visible, near infrared (NIR) and mid-IR wavelengths, as seen in Figure 4.2. This tunability has already led to the development of a new class of smart windows and has generated interest in metal oxide nanocrystals for applications such as chemical sensing and biosensing, telecommunications, and advanced optics and photonics[73-75].

Tungsten oxide (WO_3), molybdenum oxide(MoO_3), and indium oxide (In_2O_3) are among the materials that can show significant plasmonic properties in terms of oxygen

vacancy defects. Due to the strong electron affinity of oxygen, the filled valence band is

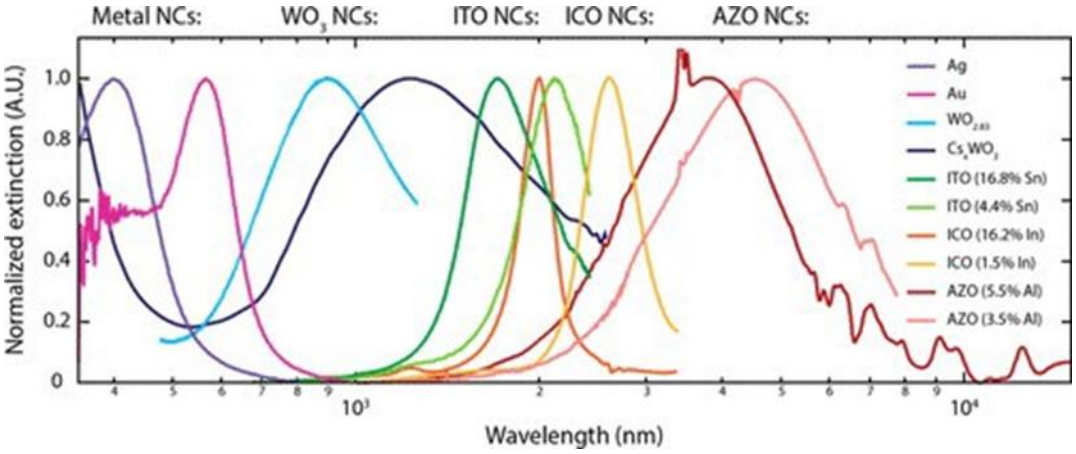

4.2. Normalized optical extinction due to LSPRs in solutions and films of metal and metal oxide nanocrystals. Oxide LSPR spectra were adapted left to right[73].

produced in oxygen orbitals and introduces two extra electrons into the conduction band, thus leaving a double defect in the lattice. This process, called self-doping in WO3 and MoO3 nanocrystals, enables the observation of LSPRs in the near infrared (NIR) of electron concentration[76,77] .

CHAPTER 5

PHOTOCATALYSIS APPLICATIONS OF TUNGSTEN OXIDE NANOSTRUCTURES

Photocatalysis can be thought of as a combination of two well-known words: catalysis, which changes the reaction rate, and photon. In photocatalysis applications, when a semiconductor material is used that can change the rate of the reaction when exposed to light; The semiconductor that absorbs light forms electron-hole pairs. The process is activated by the absorption of photons with energy corresponding to the band gap of the material used. This means that tungsten oxide can work well in the infrared and visual region because it has a band gap of 2.6-2.8 eV. With the absorption of photons, the electron moves to the conduction band, leaving a hole in the valance band. As a result of a reduction-oxidation reaction, an oxidized product is formed. Through these reduction reactions, toxic compounds become non-toxic (Figure 5.1), while pollutants such as dyes are cleared from water through oxidation reactions. This process is illustrated by the following equations (Figure5.2)[79].

$$PC + h\nu \rightarrow e^- + h^+ \quad (5.1)$$

$$h+ + H_2O \rightarrow H^+ + OH^- \quad (5.2)$$

$$h^+ ++ OH^- \rightarrow +OH \quad (5.3)$$

$$e^- + O_2 \rightarrow +O^- \quad (5.4)$$

$$2e^- + O_2 + 2H^- \rightarrow +H_2O_2 \quad (5.5)$$

$$2e^- + H_2O_2 \rightarrow OH^- + OH^- \tag{5.6}$$

$$R + OH^- \rightarrow Degradationproducts \tag{5.7}$$

$$R + h^+ \rightarrow Oxidationdegradedproducts \tag{5.8}$$

$$R + e^- \rightarrow Reductiondegradedproducts \tag{5.9}$$

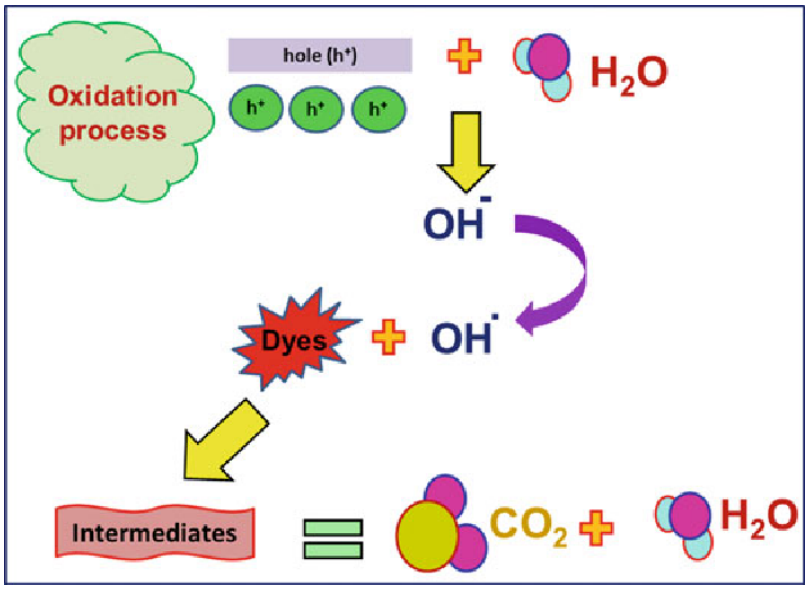

Figure 5.1. Schematic representation of oxidation mechanism

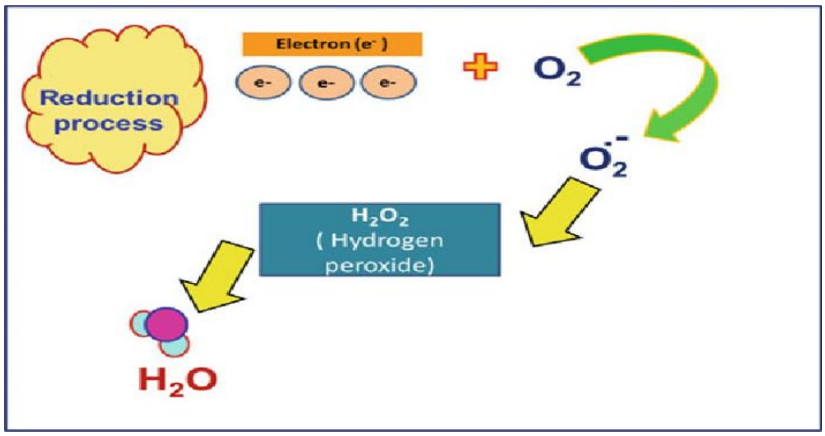

Figure 5.2. Schematic representation of reduction mechanism

5.1 Photocatalysis Investigations of Sub-Stoichiometric Tungten Oxide (WO_{3-x}) and Stoichiometric Tungten Oxide (WO_3)

It significantly increases the efficiency of photocatalysis reactions in that the oxygen vacancies in metal oxides can act as adsorption and active sites and contribute significantly to the reactivity of metal oxides[80]. Leads to the formation of unpaired electrons that can in principle form donor levels[81,82]. Cationic rhodamine B (10 mg RhB/L), which has polluting properties, was used to examine the photocatalytic activities of stoichiometric and sub-stoichiometric tungsten oxide nanowire powders. Then, 40 mg of each produced tungsten oxide powder was added to 80 ml of RhB solution. Solutions with hydrogen peroxide (H_2O_2), low pH and hydrogen peroxide at low pH were prepared. The solutions were mixed using a continuously magnetic stirring in the dark for 1 hour for adsorption stability. The dispersion was then placed under an AM 1.5 solar simulator and irradiated with a 500 W xenon lamp under conditions of continuous magnetic stirring. To determine the adsorption properties, samples were taken from the solution at specified intervals and centrifuged, and thus the photocatalytic properties of the WO_3 and WO_{3-x} photocatalysts were characterized by a UV/vis spectrometer. To examine the mechanisms of increasing photocatalytic activity and its effect on WO_3 and WO_{3-x}, photocatalytic measurements were taken with and without hydrogen peroxide as an electron acceptor. Measurements were taken in the presence of low pH and at the pH of the system itself to examine the photocatalytic effect of changing the pH of the environment, as it also

changes the reduction and oxidation potentials.

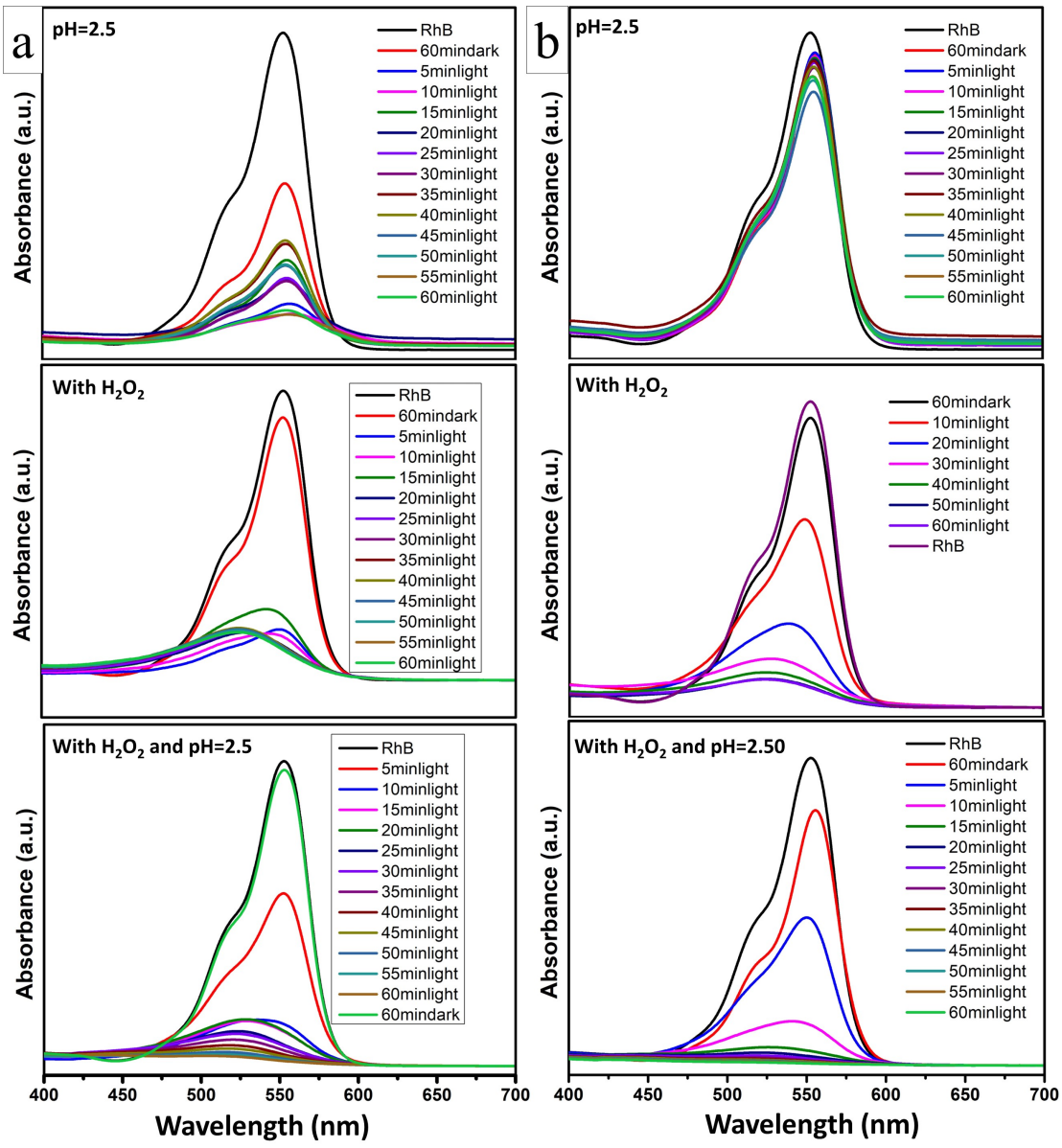

Figure 5.3. Photocatalytic properties of a) WO_{3-x}, b) WO_3

In Figure 5.3, the top graph shows the measurements taken when pH = 2.5. However, thanks to the oxygen deficiency that WO_{3-x} contains, from the first measurement it is seen that there is a faster degradation of the polluting paint compared to WO_3. While WO_{3-x} powder can break down almost 89 % of Rhodamine B (In Figure 5.3a), this rate remains only 15 % in WO_3 (In Figure 5.3b).

For photodegradation, photogenerated electrons and holes can react with adsorbed O_2 and OH, respectively, thus accelerating the system to form reactive oxygen species that

can mineralize pollutants. For this purpose, we observed how it changed the system by using H_2O_2. The results show that WO_{3-x} speeds up the system dramatically, especially after the first 10 minutes, but then it reaches saturation and remains at the same level of 11 % (middle of the In Figure 5.3a) . It is seen that H_2O_2 acts as an important electron acceptor for WO_3, while the pollutant decomposes in a balanced way, the pollutant rate decreased to 6 % at the end of 1 hour (middle of the In Figure 5.3b).

However, the most effective results were obtained by both lowering the pH and adding H_2O_2 to the solution. In the system with WO_{3-x}, the pollutant rate drops to 1.6 %, while in the system with WO_3 (the bottom graph in the Fig. 5.3 a) added, the pollutant rate drops to 0.5 %, reaching the most efficient result (the bottom graph in the Fig. 5.3 b).

5.2 Photocatalysis Investigation of Hierarchical Flower-like Sub-Stoichiometric Tungten Oxide (WO_{3-x})

It has been found that the photocatalytic properties and performances of semi-conductors are also related to the structural properties of the semiconductor. It is a feasible strategy to increase the photocatalysis performance of hierarchical semiconductor nanostructures, various hierarchical structures can be seen in Figure 5.4[83]. Hierarchical structures increase the speed and performance of photocatalysis in that they have a very large surface area in terms of collecting light, the ability of photons to pass through the pores, activating the inactive areas inside and increasing the light transfer pathways (Figure 5.5)[84]. Hierarchical nanostructures are the materials with the most efficient photocatalytic properties in utilizing light[85,86].

To characterize the photocatalytic performance of the hierarchical structure, first 80 ml of rhodamine B (10 mg RhB/L) solution was taken and 40 mg of produced hierarchical tungsten oxide powders were added into it. It was mixed with the help of a magnetic stirrer in a dark for 1 hour. No electron acceptor was added and the pH was not changed. After 1 hour, the first measurement was taken from the dark. Then, it was placed under the AM 1.5 solar simulator using a 500 W xenon lamp and measurements were taken every 20 minutes. As seen in Fig. 5.6, the hierarchical tungsten oxide managed to remove 99 percent of the pollutants from the water in the first 40 minutes.

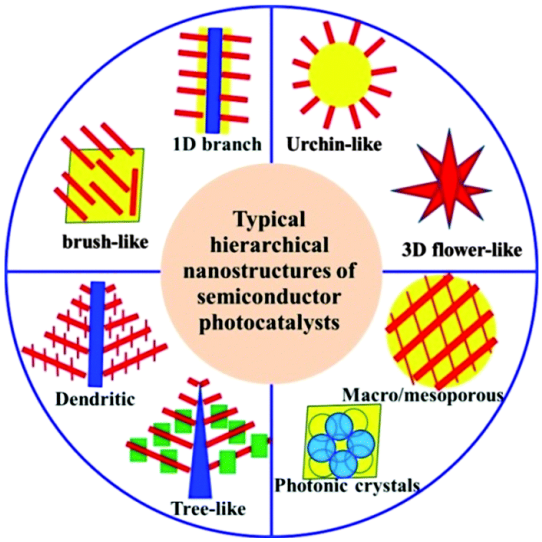

Figure 5.4. Typical hierarchical structures of photocatalysts.[83]

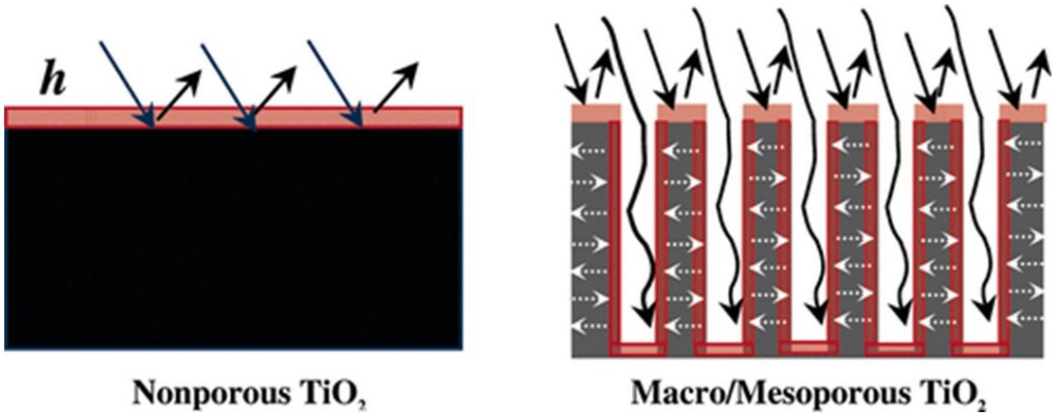

Figure 5.5. Light absorption scheme of hierarchical materials with simple micro and mesoporous structures.[84].

5.3 Photocatalytic Properties of Faceted 1D Tungsten Oxide Nanostructures

It is known that the oxygen vacancies in tungsten oxide affect photocatalysis performances and rates by showing a plasmonic effect. However, hierarchical structures have positive effects on photocatalysis performances due to their ability to absorb light well. When it is observed how the morphologies of two stoichiometric structures change the process in photocatalysis reactions (the photocatalysis procedure is the same as the structures above). Figure 5.7 shows that the sword-like structure in option b showed both faster and better performance than the flat-tipped tungsten oxide in option a. Sword-like tungsten oxide nanowires have been shown to remove 95 % of pollutants from water after

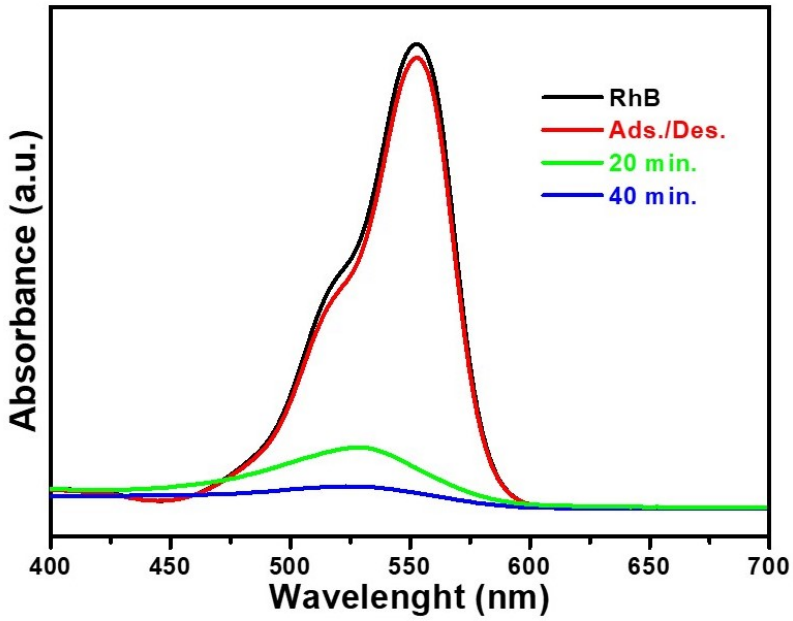

Figure 5.6. Photocatalytic properties of Hierarchical Flower-like Sub-Stoichiometric Tungten Oxide

1 hour. Figure 5.7 shows that flat-tip tangsten oxide nanowires only show a performance of 78 % after 80 minutes.

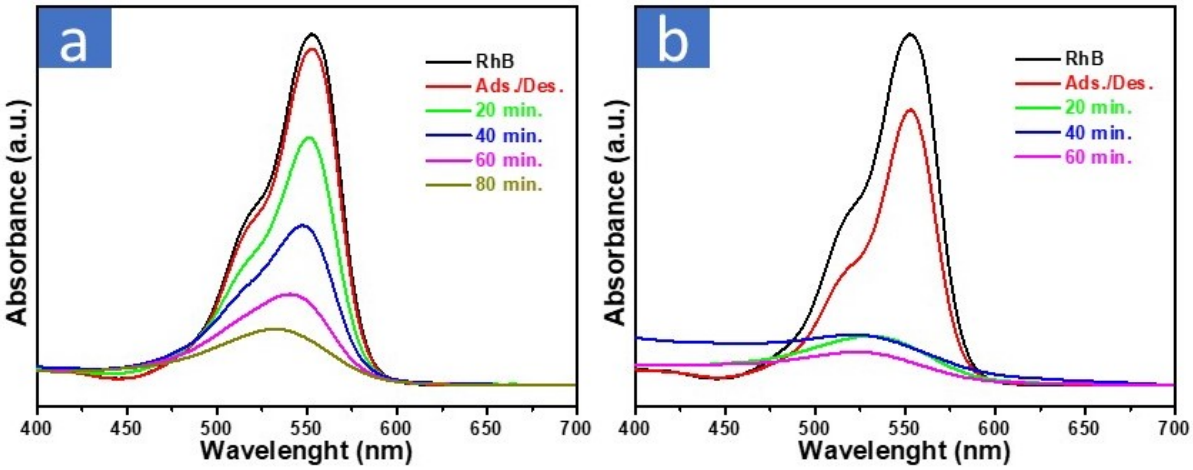

Figure 5.7. Photocatalytic properties of a) flat-tiped tungsten oxide nanowires, b)sword-like tungsten oxide nanowires

CHAPTER 6

FDTD SIMULATION FOR OPTICAL PROPERTIES OF TUNGSTEN OXIDE NANOWIRES

Finite difference time domain (FDTD) is a numerical analysis technique that models electrodynamics with associated differential equations using time-dependent Maxwell equations. After the computational domain and grid materials are designed, plane waves are used to simulate situations such as light scattering from objects or the structure of photonic bands. Figure 6.1 shows a workflow of how this modeling works. By finding out how the beam propagates through the medium by solving the Maxell equations, it ultimately helps characterize the optical properties of materials such as absorption, reflection, field distribution, refractive index, dielectric coefficients.

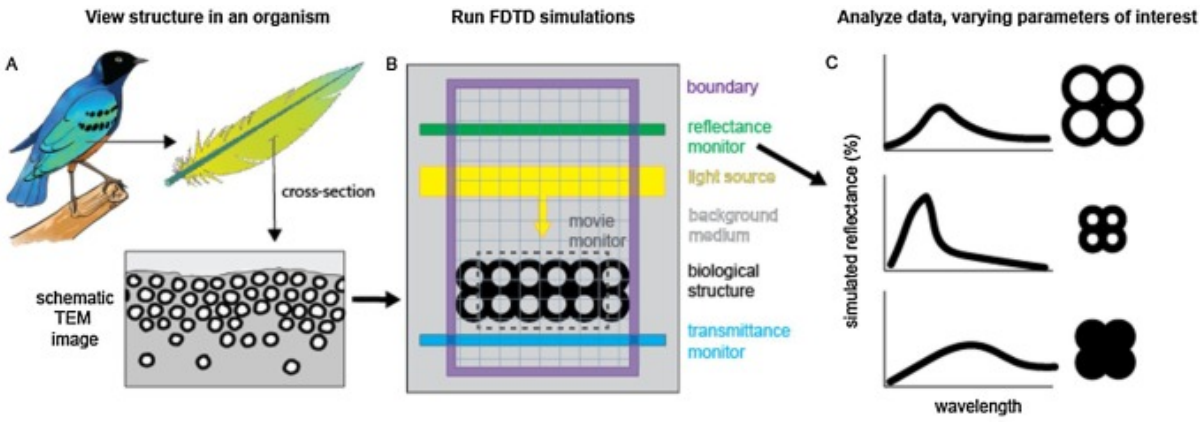

Figure 6.1. Schematic overview of the FDTD workflow[87].

6.1 FDTD Simulation

The finite difference time domain (FDTD) method was used to investigate the optical properties of WO_{3-x} (sub-stoichiometric) nanowires and WO_3 (stoichiometric)

nanowires. In the simulations, a plane wave was used. Radii obtained from SEM images were used in modeling. Since our materials consist of wires, lengths were not taken into account because there was not enough confinement along this axis.

Using Mie-Gans theory, the absorption spectrum was modeled to match the experimental data with the equation given below[**?**]. This formula includes dielectric characteristics of the medium, εm, and the nanoparticle (the real part, $(\varepsilon 1)$, and the imaginary part, $(\varepsilon 2)$ as well as depolarization factors (Pj, j=1,2,3 for x, y and z, respectively) in all three dimensions of the nanoparticle. According to this modeling, dielectric functions and refractive indices corresponding to wavelength were obtained. The field distribution was modelled to observe its behavior of the electric field at the absorption peaks.

$$A \propto \omega \varepsilon_m{}^{3/2} \sum_j \frac{\left(\frac{1}{P_j{}^2}\right)\varepsilon_2}{\left(\varepsilon_1 + \frac{1-P_j}{P_j}\varepsilon_m\right)^2 + \varepsilon_2{}^2}$$

6.1.1 Absorption Spectra of Tungsten Oxide Nanowires

Fig.6.2 shows the absorption graphs measured using the Thermo Scientific GENESY S50 spectrometer, shown with the red line. Models obtained with the Mie-Gans approach are indicated by the blue line. Using the dielectric parameters obtained from the fitting, absorption spectra the simulation results show similar results. Accordingly, in Fig. 6.2 a, there is a peak at 296 nm in the absorption graph of WO_{3-x}, while in Fig.6.2 b, there is an absorption peak at 347 nm in the absorption graph of WO_3.

6.1.2 Dielectric Constant and Refractive Indexes of Tungtsen Oxide Nanowires

The real and imaginary parts of the dielectric functions were found with the data obtained from the normalized absorption graph, by substituting the dielectric functions

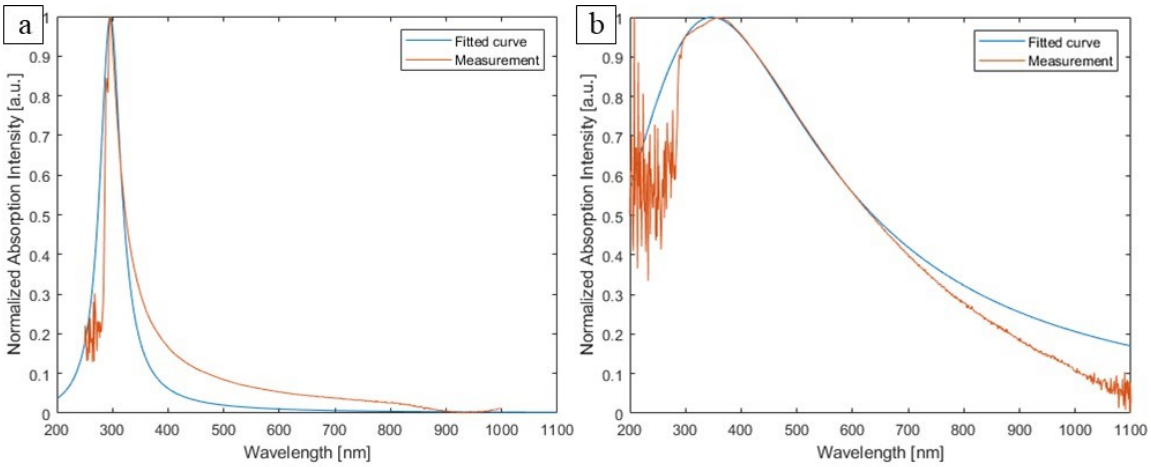

Figure 6.2. Theoritical and experimental absorption spectra of tungsten oxide nanowires

corresponding to the wavelength in the formula,

$$n_{\lambda}^{2} = n + i\kappa = \varepsilon 1 + i\varepsilon 2 \tag{6.1}$$

the real and imaginary parts of the refractive indexes of the materials were found according to the wavelength. (Fig.6.3). The dielectric functions of materials consist of two components, real and imaginary parts. The real part is defined as the ability to store and send energy and the polarization of the material, while the imaginary part is defined as the absorption and loss factor of a and b show the real and imaginary parts of the dielectric function parts of WO_{3-x} and WO_3, respectively. Accordingly, it is seen that WO_{3-x} has the ability to store and send energy better, as well as absorb it better, as can be seen from the values in both real and imaginary parts, compared to WO_3. Additionally, in Fig 6.3, the reactions of the materials to the electric field are shown where there are absorption peaks. When compared, it can be seen that the response of WO_{3-x} to the electric field at the absorption peak (at 296 nm) (Fig. 6.3 a) is more intense than that of WO_3 at the absorption peak (at 347 nm) (Fig. 6.3 b).

6.1.3 Field Distributions of Tungsten Oxide Nanowires

On the right side of Fig.6.4 a, the refractive indices of WO_{3-x} nanowires changing with wavelength are shown. While the imaginary part of the refractive index shows a

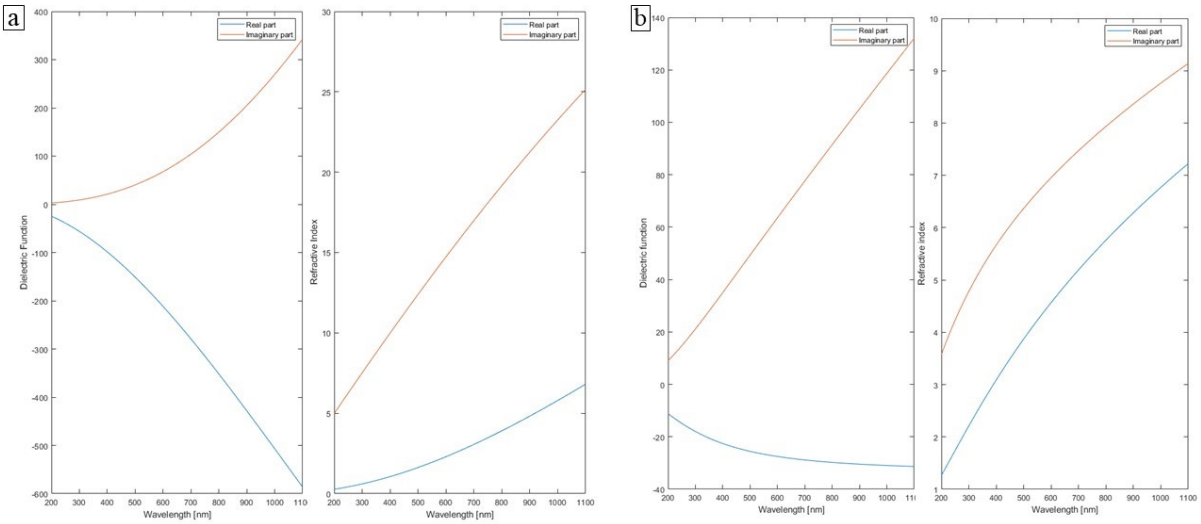

Figure 6.3. Dielectric functions and refractive indexes of Tungsten Oxide nanowires

linear increase, the real part shows non-linear behavior. On the right side of figure Fig.6.4 b, it is seen that the refractive index of WO_3 nanowires increases with the same non-linear properties in both the real and imaginary parts.

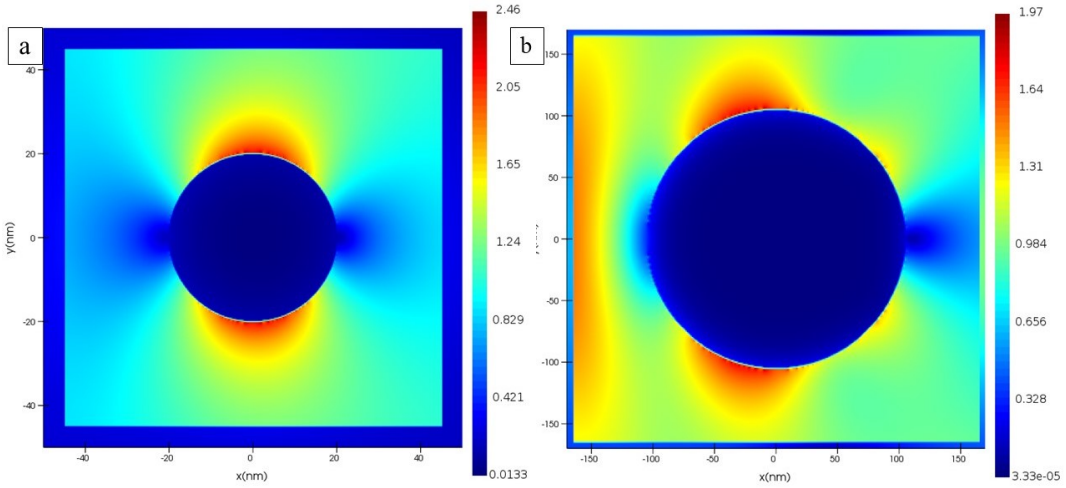

Figure 6.4. Field distribution of a)Sub-stoichiometric Tungsten Oxide nanowires, b) Stoichiometric Tungsten Oxide Nanowires

CHAPTER 7

SUPERCAPACITORS

While technologies developed for renewable energies such as wind and solar are making significant progress, there is a parallel progress in the technologies required for energy storage[88]. Supercapacitors, known as new generation energy storage sources, have faster charging and discharging ability compared to known batteries, while also having more energy storage capacity than traditional capacitors. Simply put, the working mechanisms of supercapacitors are as follows; it occurs when electric charges accumulate at the electrode and electrolyte interface, and thus energy storage depends on the surface area. There are 2 types of supercapacitors as shown in the schematic (Figure 7.1). One of them is the electochemical double layer capacitor (EDLC), which consists of carbon-based materials such as graphene, carbon foam, carbon nanotube, carbon aerogel and where the charges are stored electrostatically[89-91]. The other is the metal-oxide materials that perform the charge storage process electrochemically, which is the subject of this thesis and will be examined in detail below. There are also hybrid capacitors, which are an intermediate structure consisting of a Pseudosupercapacitor/EDCL mixture that can use both mechanisms at the same time. It is important that the cycle of hybrid capacitors is long-lasting, therefore does not require maintenance, and can be charged quickly[92,93].

The capacitance value of EDLC based on electrostatic charges is calculated with the following formula; where A is the surface area of the electrode; ϵ_0 is the permeability of free space; ϵ_r is the relative permittivity of the dielectric material; and d is the distance between the electrode.

$$C = (\epsilon_0 * \epsilon_r * A)/d \qquad (7.1)$$

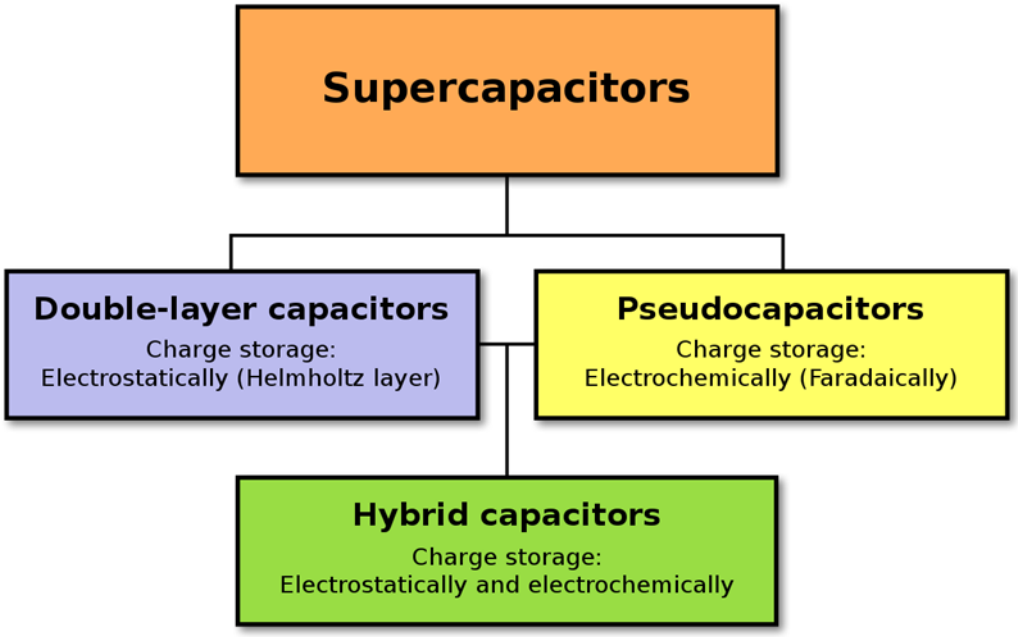

Figure 7.1. A diagram that shows a hierarchical classification of supercapacitors of related types

7.1 PSEUDOSUPERCAPACITORS

In pseudosupercapacitors, charge transfers occur in a faradic, reduction/oxidation reactions occur when ions are absorbed on the electrode, the specific capacitance for these supercapacitors depends on the number of electrons in the redox reaction, the molar mass of the metal oxide and the voltage and is calculated by the following formula (where F is the Faraday constant);

$$C = (n * F)/(M * V) \quad (7.2)$$

As can be seen from the formula 7.2 , metal oxides with low molar mass and more electrons that can be transferred have higher capacitance and play an important role in electrochemical performance[94,95].

Since the process occurs on the surface of the electrodes for the capacity of the supercapacitor, the higher the specific surface area, the more electron-active sites it will have, which is an important parameter[96,97].

Compared to metals, it is seen that the conductivity of metal oxides is lower due to their semiconductor and this is limiting in capacitance. In other words, it is clear that the smaller the band gap of the metal oxide, the better capacitance it will have. Just as capacitance is important, energy and power density of metal oxide electrodes are two important concepts in supercapacitor applications and can be found with the following formulas; where C is the capacitance in farads, V is the nominal voltage and R is the equivalent series resistance (ESR) in Ohms

$$E = (C * V^2)/2 \tag{7.3}$$

$$P = V^2/(4R) \tag{7.4}$$

When talking about supercapacitors, it is worth mentioning the widely used Ragona plot (Figure 7.2), which is basically a technique for comparing different batteries and technologies to identify the strengths and weaknesses of these technologies[99,100]. In the graph comparing the performances of various devices for storing energy, power density is on the y-axis in W/kg and represents the amount of power per unit weight of a battery, while energy density is on the x-axis and is in Wh/kg and represents the amount of energy it can store per unit weight[101]. Batteries are located in the upper right part of the chart as they have both high power and high performance. The Ragone chart is used as a communication tool for researchers, engineers, and manufacturers as advances are placed on the chart and energy-storing devices such as supercapacitors and batteries can be easily communicated to large audiences, offering broad collaboration and sharing opportunities[102,103].

7.1.1 Electrochemical Impedance Spectroscopy

One method of evaluating the impedance of a charge storage device, which is the equivalent resistance of each component or electrical circuit to current, is through Nyquist plots. It is a graph that places the real part of the impedance on the x-axis and the imaginary parts on the y-axis. The intersections on the x axis in the graph (small images in Fig 7.7) are the resistance of the electrolyte (R_b) of the supercapacitor electrodes.

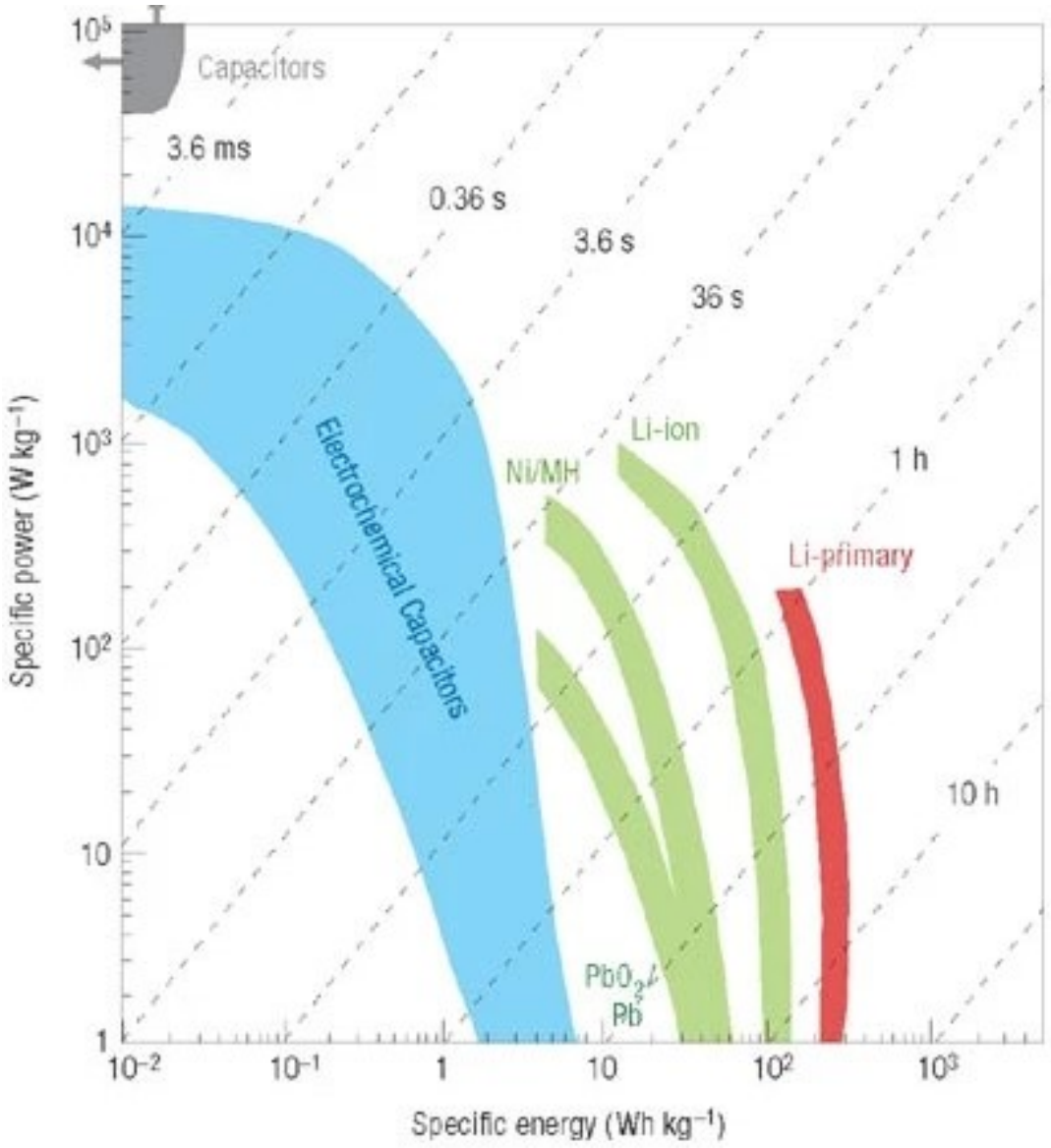

Figure 7.2. Specific power against specific energy, also called a Ragone plot, for various electrical energy storage devices. Specific power against specific energy, also called a Ragone plot, for various electrical energy storage devices[98].

Using these values, the conductivity (σ) of the electrodes is calculated as follows

$$\sigma = T/(R_b * A_e) \tag{7.5}$$

where T is the thickness of the supercapacitor, R_b is the resistance of the electrolyte and A_e is the surface area of the electrode of the supercapacitor.

7.1.2 Cyclic Voltammetry

Cyclic voltammetry measurement applies a linearly varied electrical potential between the positive and negative electrodes of a supercapacitor in a two-electrode cell configuration and is a powerful electro-chemical technique used to investigate reduction and oxidation processes of molecular species. The thermodynamics of a redox process provides important information about the kinetics of heterogeneous electron transfer reactions and the chemical reaction or adsorption that goes along with the electrode reaction. By detailed examination of cyclic voltammograms, it can be understood at what potential and in how many steps a system is reduced and oxidized, whether it is electrochemically reversible, whether the electrode reaction is related to a chemical reaction in solution, the stability of the reaction products, the existence of an adsorption and the effects of the environment on the redox process.

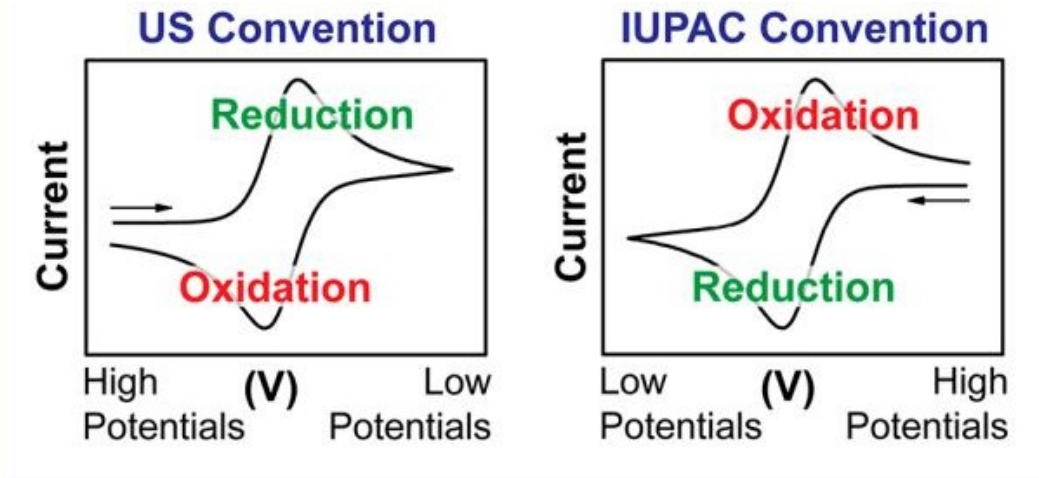

Figure 7.3. Two conventions are commonly used to report CV data [104].

7.1.3 Faradic and Non-Faradic Prosess

When performing electrochemical analysis, faradic and non-faradic processes must be examined for electrode characteristics. When Faraday's law is observed, (Equation 6.6 is the amount of charge passing through the electrode according to Faraday's law, where q, n, N and F are the amount of charge passing through the circuit, respectively, the

valency of the metal produced on the electrode, the number of moles of the substance produced and Faraday's constant.) In faradic processes, the charge on the electrode in the redox reaction transfer occurs, the charge on the electrode must not be stored in the electrode and the charge must be transferred away. In non-faradaic processes, there is no charge transfer, the charge remains on the electrode, similar to adsorption/desorption at the electrolyte-electrode interface (Figure 7.5). A non-Faradaic process is observed in the electric double-layer capacitor (EDLC)[121].

$$q = \nu * N * F \tag{7.6}$$

In pseudosupercapacitors, the faradic process dominates, the capacitance consists of fast and reversible redox reactions on the electrode[116,117]. The charge passes through the double layer, allowing faradic current to flow through the supercapacitor, a process that increases the energy density and specific capacitance[118,119].

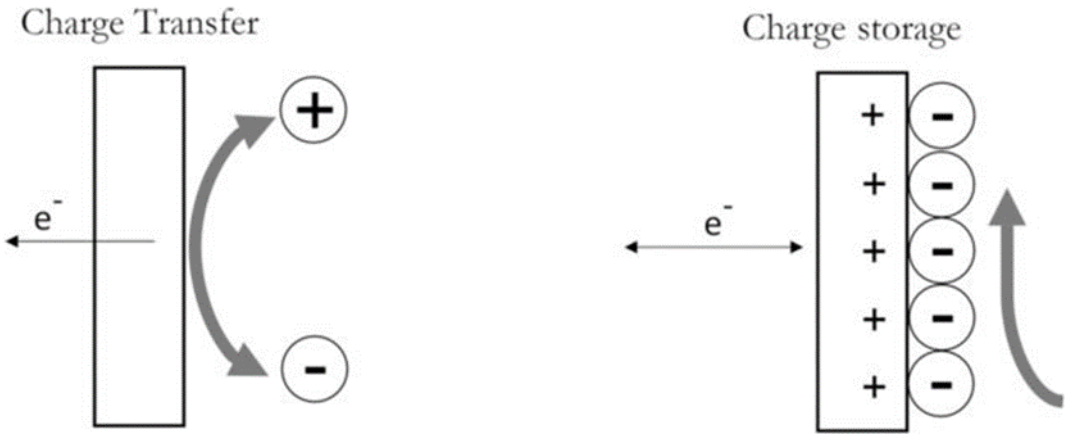

Figure 7.4. Comparison between faradaic and non-faradaic processes[120].

7.1.4 Electrolytes for Supercapacitors

An important topic affecting the performance of supercapacitors is the choice of electrolyte. Both high energy and high power density can be achieved when a suitable

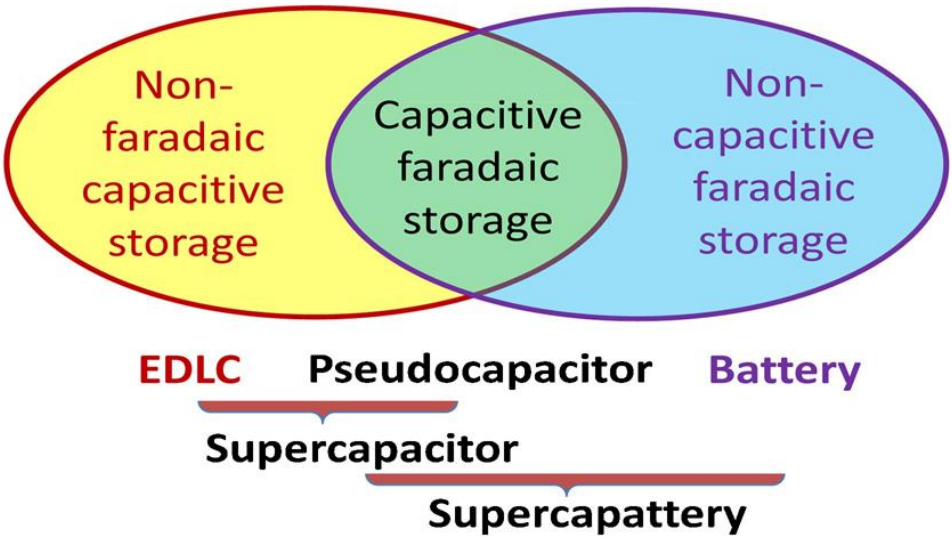

Figure 7.5. Schematic correlation between EDL capacitor, pseudocapacitor, battery and supercapattery (= hybrid of supercapacitor and battery) in terms of capacitive and faradaic charge storage processes[122].

electrolyte is selected. When selecting the electrolyte, parameters such as having electro-chemical stability and high ion concentration, low voltage and viscosity, low cost and low toxicity are sought[105].

There are three main types of electrodes used for supercapacitors. Among these, aqueous solutions are alkaline solutions (such as KOH solution), acidic solutions (such as H_2SO_4 solution) and neutral solutions (such as Li_2SO_4, Na_2SO_4 or KCl solution)[106,107]. Aqueous electrodes have a high ion concentration, so supercapacitors using aqueous solutions as electrolytes have higher capacitance and power, but aqueous solutions have a very low voltage capacity (about 1.23 V), which means they have a higher voltage window (3.5) and are therefore more durable[108,109]. Other electrolyte types, organic electrolytes (such as propylene carbonate (PC)), stand out in terms of their high energy density and higher energy density, but they have disadvantages in terms of complex preparation procedures, high toxicity, and low conductivity[110].

Finally, ionic liquids, which consist of salts that are molten at room temperature, are another type of electrolyte. Their main features are that the voltage window is 2-6 volts, they have low flammability, they have high electrochemical stability, they are non- toxic, and since ionic liquids consist of ions and do not contain solvents, this makes them very environmentally friendly electrolytes[111,112]. Their low conductivity at room temperatures is their disadvantage because it affects the electrochemical performance of the superconductor[113-115].

7.1.5 TUNGSTEN OXIDE NANOWIRES AS ELECTRODES FOR SUPERCAPACITORS

7.1.5.1 Electrochemical Measurements

Electrochemical performances and characterizations of WO_3-based electrode materials and produced symmetric and asymmetric supercapacitor (SC) devices were performed using a multi-channel BioLogic VMP 300 potentiostat in a two-electrode configuration. In order to characterize the charge storage behavior of WO_3 electrodes, 6 M KOH aqueous solution was chosen as the electrolyte. Stainless steel screws were used to collect current on both sides, and a porous glass fiber paper (Whatman,grade GF/F) heated with the selected electrolyte was used as a separator. The synthesized WO_3 powders were used directly as electrodes for asymmetric and symmetric SC devices without any processing, and no binders or additives were used in the preparation of these electrodes. All tests were carried out at room temperature with the help of cyclic voltammetry (CV), potentiostatic electrochemical impedance spectroscopy (PEIS or EIS) and potential-limited galvanostatic cycling (GCPL) techniques. For CV characterization, 20 cycles were recorded by selecting various scan rates from 10 to 200 mV.s^{-1} in the voltage range from 0 to +1 V. For GCPL measurements, 50 cycles were performed at currents of 0.1 A/g, 0.15 A/g, 0.2 A/g, 0.3 A/g, 0.50 A/g and 2.40 A/g (at a scan rate of 100 mV/s).

7.1.5.2 Electrochemical Properties and Supercapacitor Performance Test

For electrochemical measurements and supercapacitor performance tests, symmetrical devices (WO_{3-x} and WO_{3-x}) (WO_3 and WO_3)in which both electrodes consist of the same material and asymmetric devices with different electrodes were designed (WO_{3-x} and WO_3). According to the measurements taken in the symmetrical two-electrode cell configuration, when the scanning speeds are changed to 10, 20, 50, 100, 200 mvs^{-1}, as seen in Fig. 7.6 there is a linear increase in all three designed devices (voltage and current increase as the scanning speeds increase) and this linear behavior indicates that the system has faradic properties. Although faradic processes show electron transfer at the interface between the electrolyte and electrode, faradic processes alone do not give us

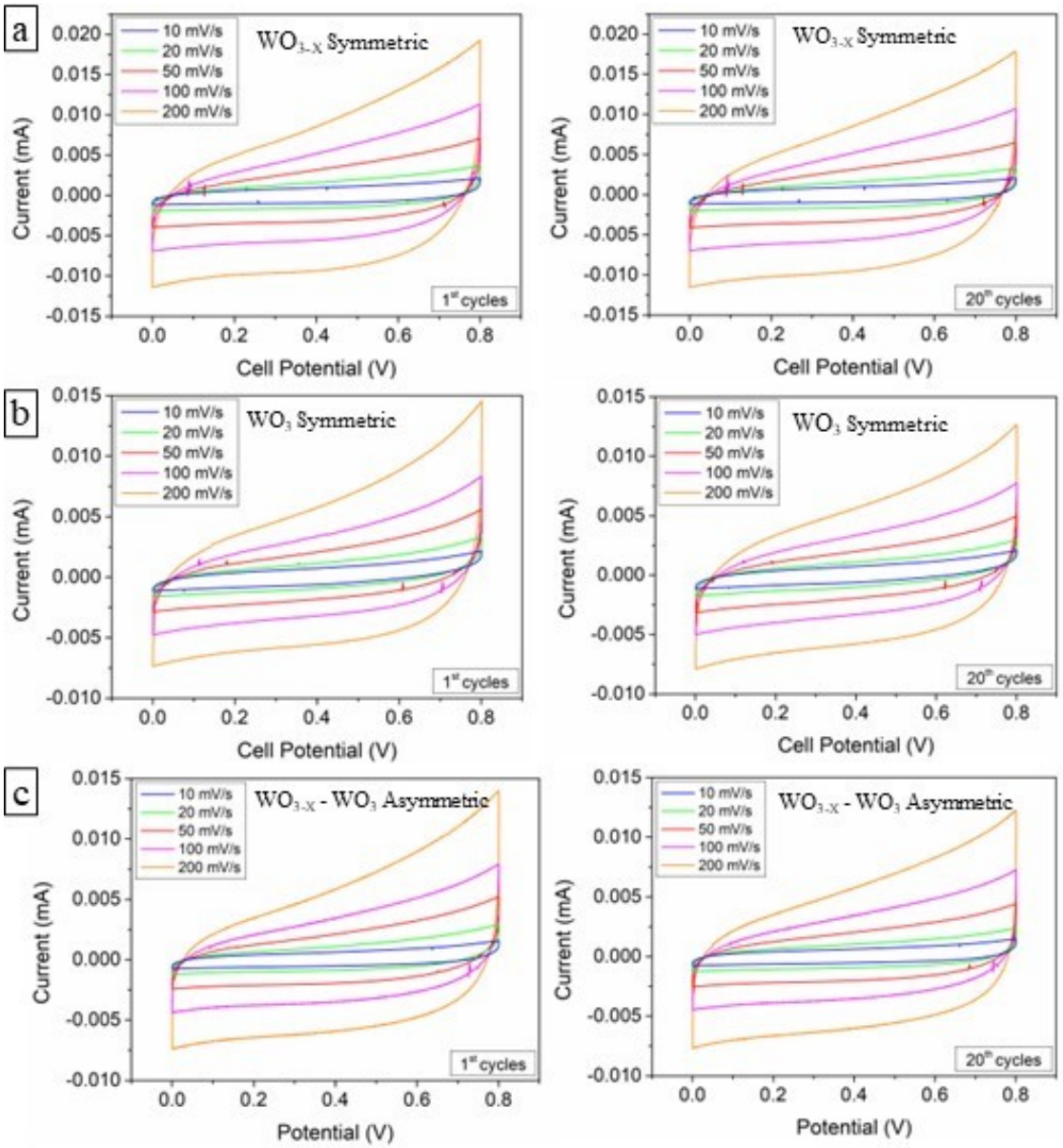

Figure 7.6. Cyclic Voltammetry of Tungsten Oxide Nanowires carried out between 0 and 1 V with different scan rates

precise information about electron transfer, redox reactions, and charge storage that may be valid for the pseudocapacitor.

Impedance, which consists of two components: real/resistive (Zreal) and imaginary/capacitive (Zim), plays an important role in characterizing the frequency behavior of supercapacitors. Nyquist plots characterizing impedance measurements are divided into two regions for supercapacitor applications, the low frequency region is characterized by a linear curve while the high frequency region is characterized by a semicircle. It is the indicator of the faradaic process occurring at the interface of the semicircular electrode and electrolyte in the high frequency region, and is the combination of electrochemical double layer capacitance and charge transfer resistance. Accordingly, in the symmetrical

two-electrode systems in the left and middle in Fig. 7.7, no semicircle could be observed in the high frequency region. The reason for this may be spurious capacitance or fast charge transfer processes occurring at the electrode and electrolyte interface. However, in the two-electrode system, the asymmetric system with one end WO_{3-x} and the other end WO_3 seems more promising.

The charge-discharge rates for all three devices were increased to 0.10, 0.15, 0.20, 0.30, 0.50 and 2.40 $A.g^{-1}$, and in fig.7.8 a, the decrease in the specific discharge capacity is seen as the increase from 0.10 to 2.40 $A.g^{-1}$ is observed, and the highest discharge capacity and long It is seen that the long-term cycle performance is at 0.15 $A.g^{-1}$. Thus, as seen in fig. 7.8 b, when tested for 50 cycles at a current density of 0.15 $A.g^{-1}$ in all three electrolytes, it is seen that all three electrodes exhibit stability in the cycle by preserving 98 % of the initial capacities.

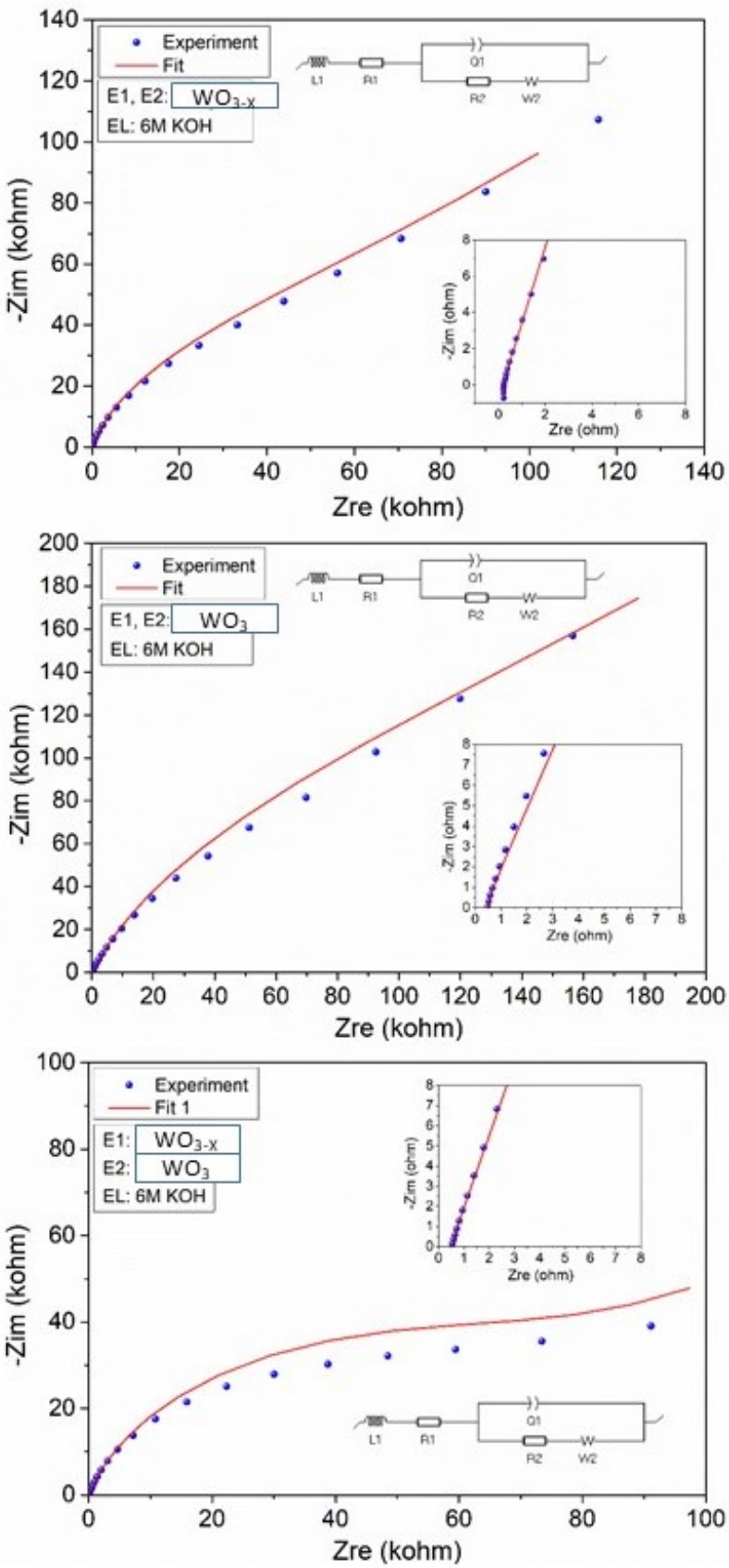

Figure 7.7. PEIS (Nyquist) graphs for Symmetric and Asymmetric Supercapacitors

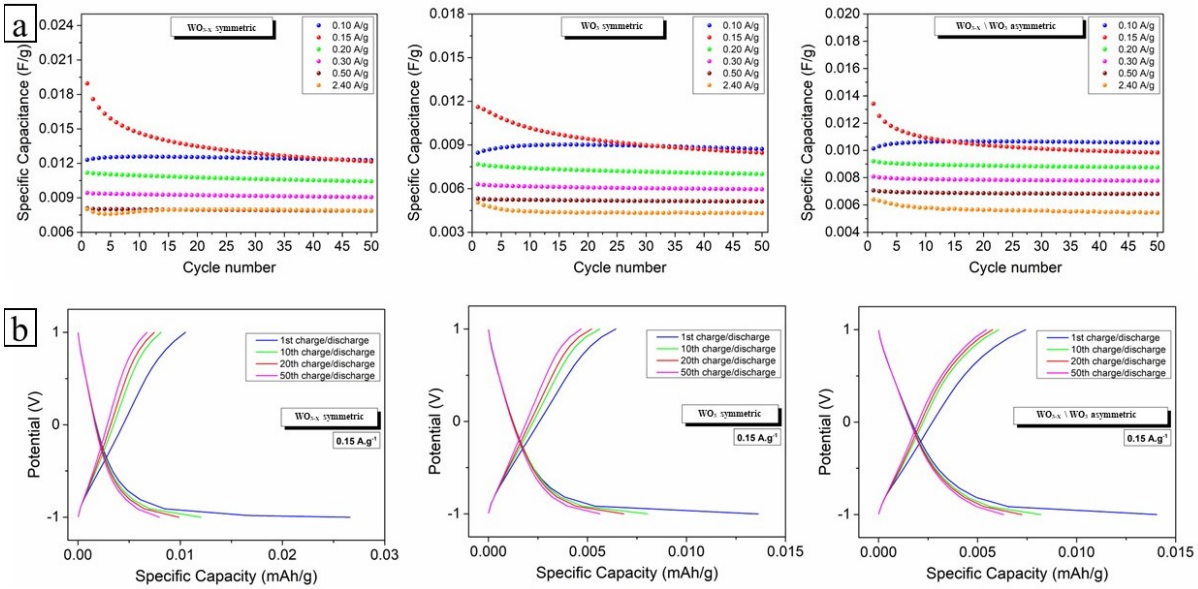

Figure 7.8. a) Cycling stability of tungstan oxide nanowires at current densities of 0.10, 0.15, 0.20, 0.30, 0.50 and 2.40 A.g^{-1}, b) specific discharge capacitances for symmetric WO_{3-x}, symmetric WO_3, and asymmetri WO_{3-x}/WO_3 nanowires.

CHAPTER 8

ELECTROCHROMIC DEVICES USING TUNGSTEN OXIDE

Materials that can change their optical properties in response to an external stimulus are called "chromogenic"[124]. Electrochromic materials, which can change their optical properties with the application of an electrical voltage, have attracted much attention in recent years[125]. With the use of electrochromic materials in glasses, the concept of smart windows with variable transmittance has begun to be seen as an important step in ensuring energy efficiency, and electrochromic materials have begun to be seen as a subset of solar energy materials[126].

When an electric field is applied to electrochromic materials, electrochemical oxidation/reduction occurs, resulting in changes in the optical band gap, which is reflected in the observed color changes. Figure 8.1 shows a typical electrochromic device design. For good stability and EC performance, there must be good electrical conduction between the layers. For this reason, there are conductive layers at the outermost part of the structure consisting of at least 5 layers[127-129]. These are materials with high conductivity such as FTO, ITO, and there are new developments open to development such as silver nanowires. The next layer consists of electrochromic material, then the ion-conducting layer (electrolyte), then the ion-storing layer, and the last layer is the transparent conductor.

In electrochromism, the coloration efficiency (CE) is a very important parameter and is equal to the optical density change (ΔOD) divided by the added charge (Qc) per area (A). The optical density change is defined by the logarithm of the ratio between the transmission of the bleached (Tb) and colored (Tc) states

$$CE\ (\eta) = (\Delta OD)/(Q/A) \tag{8.1}$$

$$\Delta OD = log(T\ b/T\ c) \tag{8.2}$$

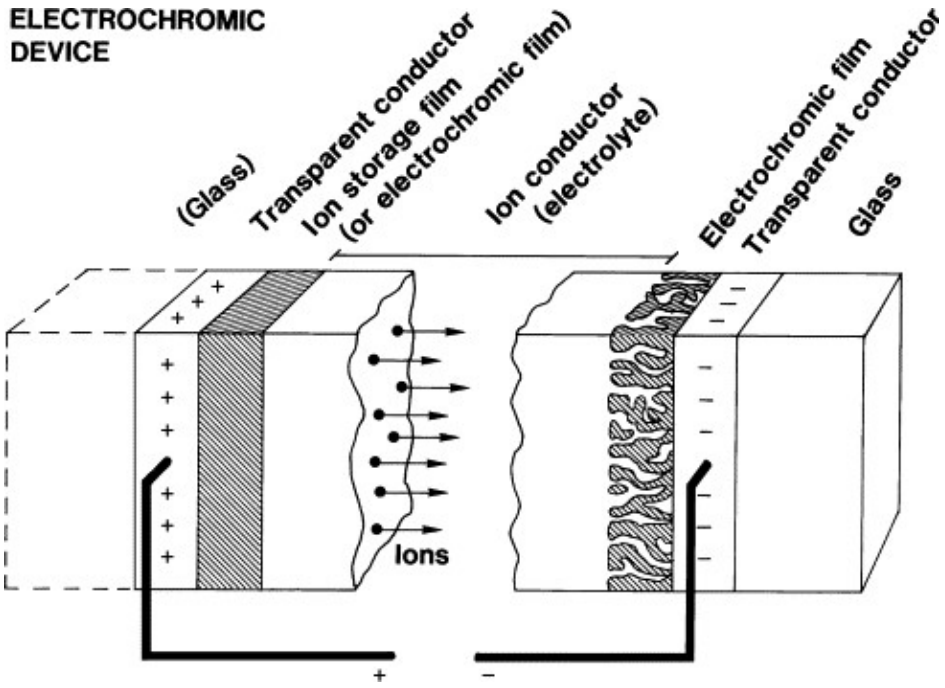

Figure 8.1. Basic design of an electrochromic device, indicating transport of positive ions under the action of an electric field.

8.1 Electrochromic Properties of WO_{3-x}, WO_3, and $CoWO_4$ Nanowires

The electrochromic effects of cobalt doping, stoichiometric tungsten oxide, and non-stoichiometric tungsten oxide with oxygen vacancies will be comparatively examined in this section. In the devices prepared for all three structures, FTO was used as the conductive layer, tungsten oxide was used as the electrochromic layer, and liquid crystal was used as the electrolyte, thus enabling the active movement of protons. To increase conductivity, devices were created using PEDOT-PSS as an intermediate layer.

While creating the electrochromic devices, a mixture of 400 microliters of water and 400 microliters of isopropanol was used as a solvent. After 50 mg of each sample was dissolved in this solvent with the help of a sonicator, pedot-pss was added as half of this mixture and coated on FTO with the help of a spin coater at 2000 rpm. The devices were heated at 120 degrees. It was annealed for 10 minutes.

The results obtained are seen in figure 8.2. In Figure 8.2, the red lines are the data taken at 2 V, and the blue lines show the potentials at 0 V. As a result of coating, sub-stoichiometric tungsten oxide nanowires have a maximum peak at 638 nm and a 33 % decrease in permeability is observed when a voltage of 2 volts is applied. In stoichiometric tungsten oxide nanowires, although their permeability is 55 % when coated, they respond only 12 % to a voltage of 2 volts. The cobalt-doped structure is better

coated on FTO because its particles are very small, and therefore it is the structure with the highest permeability, but it also has the least color change, approximately 8 %. As a result, although all three tungsten oxide structures can work electrochromically, the sub-stoichiometric structure appears to be the best working device due to the oxygen vacancies it has.

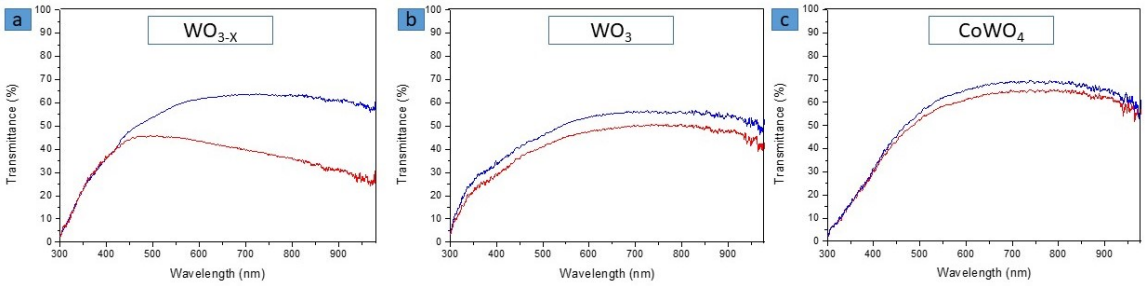

Figure 8.2. graph of tranmittance of a)sub-stoichiometric WO_{3-x} b)stoichiometric WO_3 nanowires c) CoWO_34 nanowires

In Figure 8.3, visible color changes of the created devices are seen at 0 V before the potential is applied and after the 2 V potential is applied. However, it is clear that the results will be discussed more clearly in cases where the coating will be better and optimized, and it is still a subject open to development.

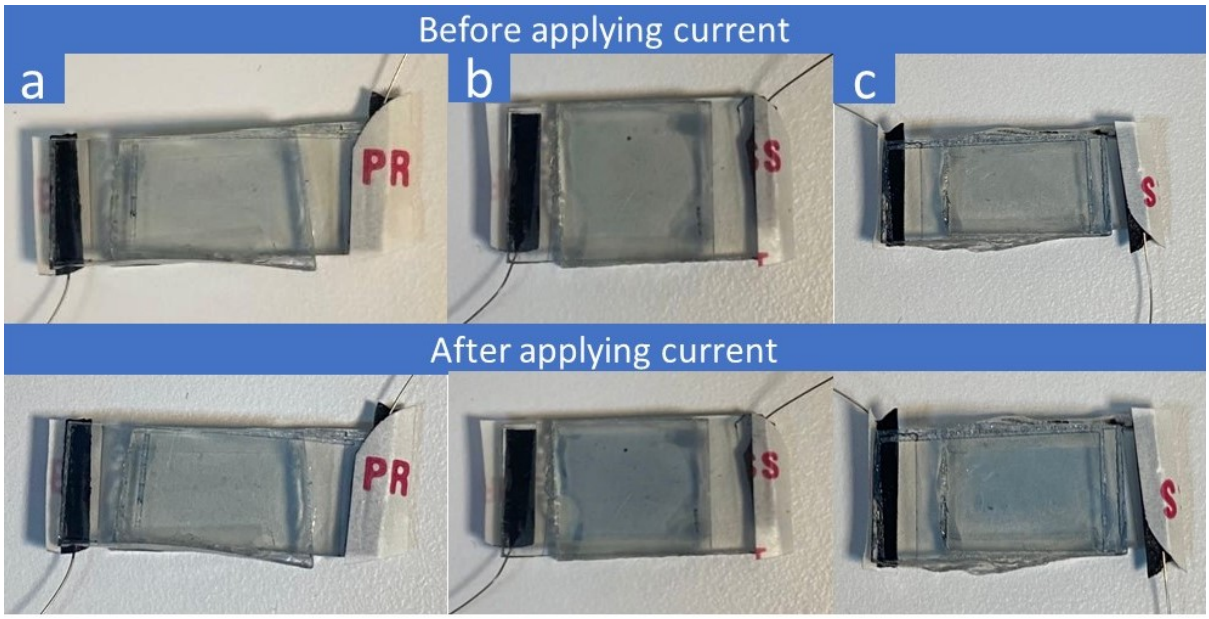

Figure 8.3. a)CoWO_4, b) sub-stoichiometric WO_{3-x}, c)stoichiometric WO_3 nanowires.

CHAPTER 9

CONCLUSION

Within the scope of this thesis, using the hydrothermal method as the synthesis method, stoichiometric tungsten oxide nanowires, non-stoichiometric tungsten oxide nanowires with plasmonic properties with oxygen gaps, hierarchical tungsten oxide structures with flower-like structure, and finally sword-like and flat-tipped nanowires were synthesized and grouped according to appropriate application areas. . Using characterization techniques such as SEM and XRD, tungsten oxides were first characterized according to their structure and phases.

Non-stoichiometric and stoichiometric nanowires were studied for photocatalysis applications and it was seen that the structure with oxygen vacancies showed faster and more effective performance until a certain saturation was reached. Hierarchically structured tungsten oxide works very efficiently and quickly due to its ability to absorb light well due to its structure and the oxygen gaps in its structure. When examined according to their morphology, it was seen that the sword-like structure was faster and had higher photocatalysis performance.

Stoichiometric and non-stoichiometric nanowires were examined in terms of their optical properties with the help of FDTD simulation. Firstly, considering the experimental absorption graph, the theoretical absorption graph was drawn with the Mie-Gans approach and it is seen that they are compatible. Dielectric functions and refractive indices of the two structures were found with the help of absorption graph. According to the field distribution graph, it is seen that non-stoichiometric tungsten oxide responds more to the electric field.

Supercapacitor applications for tungsten oxide and their performance in electrochromic applications were examined.

REFERENCES

(1) Rao, C. N. R. Transition metal oxides. *Annual Review of Physical Chemistry* **1989**, 40(1), 291-326.

(2) Patzke, G. R.; Krumeich, F.; Nesper, R. Oxidic nanotubes and nanorods—anisotropic modules for a future nanotechnology. *Angewandte Chemie International Edition* **2002**, 41(14), 2446-2461.

(3) Rao, C. N. R.; Deepak, F. L.; Gundiah, G.; Govindaraj, A. Inorganic nanowires.*Progress in Solid State Chemistry* **2003**, 31(1-2), 5-147.

(4) Tokura, Y.; Nagaosa, N. Orbital physics in transition-metal oxides. *Science* **2000**, 288(5465), 462-468.

(5) Emeline, A. V.; Kataeva, G. V.; Panasuk, A. V.; Ryabchuk, V. K.; Sheremetyeva, N. V.; Serpone, N. Effect of surface photoreactions on the photocoloration of a wide band gap metal oxide: Probing whether surface reactions are photocatalytic. *The Journal of Physical Chemistry B* **2005**, 109(11), 5175-5185.

(6) Gutowski, M.; Jaffe, J. E.; Liu, C. L.; Stoker, M.; Hegde, R. I.; Rai, R. S.; Tobin, P. J. Thermodynamic stability of high-K dielectric metal oxides ZrO_2 and HfO_2 in contact with Si and SiO_2. *Applied Physics Letters* **2002**, 80(11), 1897-1899.

(7) Chen, P. C.; Shen, G.; Sukcharoenchoke, S.; Zhou, C. Flexible and transparent super-capacitor based on In_2O_3 nanowire/carbon nanotube heterogeneous films. *Applied Physics Letters* **2009**, 94(4).

(8) Su, X.; Zhang, Z.; Zhu, M. Melting and optical properties of ZnO nanorods. *Applied physics letters* **2006**, 88(6).

(9) Devan, R. S.; Patil, R. A.; Lin, J. H.; Ma, Y. R. One-dimensional metal-oxide nanostructures: recent developments in synthesis, characterization, and applications. *Advanced Functional Materials* **2016**, 22(16), 3326-3370.

(10) Zavabeti, A.; Ou, J. Z.; Carey, B. J.; Syed, N.; Orrell-Trigg, R.; Mayes, E. L.; Daeneke, T. A liquid metal reaction environment for the room-temperature synthesis of atomically thin metal oxides. *Science* **2017**, 358(6361), 332-335.

(11) Wang, Y.; Jiang, X.; Xia, Y. (2003). A solution-phase, precursor route to polycrystalline SnO_2 nanowires that can be used for gas sensing under ambient conditions. *Journal of the American Chemical Society* **2003**, 125(52), 16176-16177.

(12) Rosario, R.; Gust, D., Garcia; A. A., Hayes; M., Taraci; J. L.; Clement, T.; Picraux, S. T. Lotus effect amplifies light-induced contact angle switching. *The Journal of Physical Chemistry B* **2004**, 108(34), 12640-12642.

(13) Zhu, K.; Vinzant, T. B.; Neale, N. R.; Frank, A. J. Removing structural disorder from oriented TiO_2 nanotube arrays: reducing the dimensionality of transport and recombination in dye-sensitized solar cells. *Nano letters* **2007**, 7(12), 3739-3746.

(14) Chen, P. C.; Shen, G.; Sukcharoenchoke, S.; Zhou, C. Flexible and transparent super- capacitor based on In_2O_3 nanowire/carbon nanotube heterogeneous films.*Applied Physics Letters* **2009**, 94(4).

(15) He, Y.; Wang, D. Toward practical solar hydrogen production. *Chem* **2018**, 4(3), 405-408.

(16) Heo, Y. W.; Tien, L. C.; Kwon, Y.; Norton, D. P.; Pearton, S. J.; Kang, B. S.; Ren, F. Depletion-mode ZnO nanowire field-effect transistor. *Applied Physics Letters* **2004**, 85(12), 2274-2276.

(17) Nguyen, P.; Ng, H. T.; Yamada, T.; Smith, M. K.; Li, J.; Han, J.; Meyyappan, M. Direct integration of metal oxide nanowire in vertical field-effect transistor. *Nano Letters* **2004**, 4(4), 651-657.

(18) Pan, J.; Dong, Z.; Wang, B.; Jiang, Z.; Zhao, C.; Wang, J.; Li, C. The enhancement of photocatalytic hydrogen production via Ti3+ self-doping black TiO_2/g-C_3N_4 hollow core-shell nano-heterojunction. *Applied Catalysis B: Environmental* **2019**, 242, 92-99.

(19) Alp, E.; Eşgin, H.; Kazmanlı, M. K.; Genc, A. Synergetic activity enhancement in 2D CuO-Fe2O3 nanocomposites for the photodegradation of rhodamine B. *Ceramics International* **2019**,9174-9178.

(20) Yan, J.; Wang, T.; Wu, G.; Dai, W.; Guan, N.; Li, L.; Gong, J. Tungsten oxide single crystal nanosheets for enhanced multichannel solar light harvesting. *Advanced Materials* **2015**, 27(9), 1580-1586.

(21) Li, S.; Xia, M.; Xiao, C.; Zhang, X.; Yu, H.; Zhang, L.; Shu, J. Common ion effect enhanced Prussian blue analogues for aqueous ammonium ion storage. *Dalton Transactions* **2021**, 50(19), 6520-6527.

(22) Peng, Y. K.; Tsang, S. E. Facet-dependent photocatalysis of nanosize semiconductive metal oxides and progress of their characterization. *Nano Today* **2018**, 18, 15-34.

(23) Fujishima, A.; Honda, K. Electrochemical photolysis of water at a semiconductor electrode. Nature 1972, 238(5358), 37-38.

(24) Yu, J.; Low, J.; Xiao, W.; Zhou, P.; Jaroniec, M. Enhanced photocatalytic CO2-reduction activity of anatase TiO2 by coexposed 001 and 101 facets. Journal of the American Chemical Society 2014, 136(25), 8839-8842.

(25) Zhang, L.; Doyle-Davis, K.; Sun, X. Pt-Based electrocatalysts with high atom utilization efficiency: from nanostructures to single atoms. Energy & Environmental Science 2019, 12(2), 492-517.

(26) Tian, B.; Tian, B.; Smith, B.; Scott, M. C.; Hua, R.; Lei, Q.; Tian, Y. Supported black phosphorus nanosheets as hydrogen-evolving photocatalyst achieving 5.4 energy conversion efficiency at 353 K. *Nature communications*, **2018**, 9(1), 1397

(27) Zhou, D.; Liu, D.; Xu, W.; Yin, Z.; Chen, X.; Zhou, P.; Song, H. Observation of considerable upconversion enhancement induced by Cu2–x S plasmon nanoparticles. *ACS nano* **2016**, 10(5), 5169-5179.

(28) Paik, T.; Cargnello, M.; Gordon, T. R.; Zhang, S.; Yun, H.; Lee, J. D.; Murray, C. B. Photocatalytic hydrogen evolution from substoichiometric colloidal WO_{3-x} nanowires. *ACS Energy Letters* **2018**, 3(8), 1904-1910.

(29) Deb, S. K. A novel electrophotographic system. *Applied Optics* **1969**, 8(101), 192-195.

(30) Salunkhe, R. R.; Jang, K.; Lee, S. W.; Yu, S.; Ahn, H. Binary metal hydroxide nanorods and multi-walled carbon nanotube composites for electrochemical energy storage applications. *Journal of Materials Chemistry* **2012**, 22(40), 21630-21635.

(31) Raza, W.; Ali, F.; Raza, N.; Luo, Y.; Kim, K. H.; Yang, J.; Kwon, E. E. Recent advancements in supercapacitor technology. *Nano Energy* **2018**, 52, 441-473.

(32) Kou, L.; Huang, T.; Zheng, B.; Han, Y.; Zhao, X.; Gopalsamy, K.; Gao, C. Coaxial wet-spun yarn supercapacitors for high-energy density and safe wearable electronics. *Nature communications* **2014**, 5(1), 3754.

(33) Carter, R.; Cruden, A.; Hall, P. J. Optimizing for efficiency or battery life in a battery/supercapacitor electric vehicle. *IEEE Transactions on Vehicular Technology* **2012**, 61(4), 1526-1533.

(34) Ke, Q.; Wang, J. Graphene-based materials for supercapacitor electrodes–A review. *Journal of Materiomics* **2016**, 2(1), 37-54.

(35) An, C.; Zhang, Y.; Guo, H.; Wang, Y. Metal oxide-based supercapacitors: progress and prospectives. *Nanoscale Advances* **2019**, 1(12), 4644-4658.

(36) Salunkhe, R. R.; Kaneti, Y. V.; Yamauchi, Y. Metal–organic framework-derived nanoporous metal oxides toward supercapacitor applications: progress and prospects. *ACS nano* **2017**, 11(6), 5293-5308.

(37) Kochuveedu, S. T.; Jang, Y. H.; Kim, D. H. A study on the mechanism for the interaction of light with noble metal-metal oxide semiconductor nanostructures for various photophysical applications. *Chemical Society Reviews* **2013**, 42(21), 8467-8493.

(38) Mortimer, R. J. Electrochromic materials. *Chemical Society Reviews* **1997**, 26(3), 147-156.

(39) Somani, P. R.; Radhakrishnan, S. J. M. C. Electrochromic materials and devices: present and future. *Materials chemistry and physics* **2003**, 77(1), 117-133.

(40) Faughnan, B. W.; Crandall, R. S.; Lampert, M. A. Model for the bleaching of WO3 electrochromic films by an electric field. *Applied Physics Letters* **1975**, 27(5), 275-277.

(41) Granqvist, C. G. Electrochromic tungsten oxide films: review of progress 1993–1998. *Solar Energy Materials and Solar Cells* **2000**, 60(3), 201-262.

(42) Monk, P. M. The effect of ferrocyanide on the performance of heptyl viologen- based electrochromic display devices. *Journal of Electroanalytical Chemistry* **1997**, 432(1-2), 175-179.

(43) Rauh, R. D. Electrochromic windows: an overview. *Electrochimica Acta* **1999**, 44(18), 3165-3176.

(44) Deb, S. K. Opportunities and challenges in science and technology of WO3 for electrochromic and related applications. *Solar Energy Materials and Solar Cells* **2008**, 92(2), 245-258.

(45) Guven, N.; Camurlu, P. Electrosyntheses of anthracene clicked poly (thienylpyrrole) s and investigation of their electrochromic properties. *Polymer* **2015**, 73, 122-130.

(46) Mortimer, R. J.; Dyer, A. L.; Reynolds, J. R. Electrochromic organic and polymeric materials for display applications. *Displays* **2006**, 27(1), 2-18.

(47) Schirmer, O. F.; Wittwer, V.; Baur, G.; Brandt, G. Dependence of WO 3 electrochromic absorption on crystallinity. *Journal of the Electrochemical Society* **1977**, 124(5), 749.

(48) Thakur, V. K.; Ding, G.; Ma, J.; Lee, P. S.; Lu, X. Hybrid materials and poly- mer electrolytes for electrochromic device applications. *Advanced materials* **2012**, 24(30), 4071-4096.

(49) Zhang, B.; Xu, C.; Xu, G.; Tan, S.; Zhang, J. Amorphous titanium dioxide film with improved electrochromism in near-infrared region. *Optical Materials* **2019**, 89, 191-196.

(50) Wu, W.; Wang, M.; Ma, J.; Cao, Y.; Deng, Y. Electrochromic metal oxides: recent progress and prospect. *Advanced Electronic Materials* **2018**, 4(8), 1800185.

(51) Assis, L. M. N. D.; Andrade, J. R. D.; Santos, L. H. E.; Motheo, A. D. J.; Hajduk, B.; Łapkowski, M.; Pawlicka, A. Spectroscopic and microscopic study of Prussian blue film for electrochromic device application. *Electrochimica Acta* **2015**, 175, 176-183.

(52) De Simone, B. C.; Alberto, M. E.; Marino, T.; Russo, N.; Toscano, M. The Contribution of Density Functional Theory to the Atomistic Knowledge of Electrochromic Processes. *Molecules* **2021**, 26(19), 5793.

(53) Moser, M. L.; Li, G.; Chen, M.; Bekyarova, E.; Itkis, M. E.; Haddon, R. C. Fast electrochromic device based on single-walled carbon nanotube thin films. *Nano letters* **2016**, 16(9), 5386-5393.

(54) Ho, K. C. Cycling and at-rest stabilities of a complementary electrochromic device based on tungsten oxide and Prussian blue thin films. *Electrochimica acta* **1999**, 44(18), 3227-3235.

(55) Jelle, B. P.; Hagen, G. Performance of an electrochromic window based on polyaniline, prussian blue and tungsten oxide. *Solar Energy Materials and Solar Cells* **1999**, 58(3), 277-286.

(56) Sarisozen, S.; Polat, N.; Mert Balci, F.; Guvenc, C. M.; Kocabas, C.; Yaglioglu, H. G.; Balci, S. Strong coupling of carbon quantum dots in liquid crystals. *The Journal of Physical Chemistry Letters* **2022**, 13(16), 3562-3570.

(57) O'hare, D. Hydrothermal synthesis. *Encyclopedia of Materials: Science and Technology* **2001**, 3989-3992.

(58) Marturi, N. Vision and visual servoing for nanomanipulation and nanocharacterization in scanning electron microscope. *Doctoral dissertation, Université de Franche-Comté* **2013**.

(59) Murray, W. A., and Barnes, W. L. Plasmonic materials. *Advanced materials*, **2007**

19(22), 3771-3782.

(60) Powell, C. J., and Swan, J. B. Origin of the characteristic electron energy losses in aluminum. *Physical Review*, **1959** 115(4), 869.

(61) Maier, S. A., and Atwater, H. A. Plasmonics: Localization and guiding of electromagnetic energy in metal/dielectric structures. *Journal of applied physics*, **2005** 98(1).

(62) Bozhevolnyi, S. I., Volkov, V. S., Devaux, E., Laluet, J. Y., and Ebbesen, T. W. Channel plasmon subwavelength waveguide components including interferometers and ring resonators. *Nature* **2006**, 440(7083), 508-511.

(63) Kildishev, A. V.,and Shalaev, V. M. Engineering space for light via transformation optics. *Optics letters* **2008**, 33(1), 43-45.

(64) Xiong, Y., Liu, Z., and Zhang, X. A simple design of flat hyperlens for lithography and imaging with half-pitch resolution down to 20 nm. *Applied Physics Letters* **2009**, 94(20).

(65) Mayer, K. M., and Hafner, J. H. Localized surface plasmon resonance sensors. *Chemical reviews* **2011**, 111(6), 3828-3857.

(66) Ehrenreich, H., and Spaepen, F. *Solid state physics* **2001**. Academic Press.

(67) Kreibig, U., and Vollmer, M. Optical properties of metal clusters (Vol. 25). *Springer Science & Business Media* **2013**.

(68) Drachev, V. P., Chettiar, U. K., Kildishev, A. V., Yuan, H. K., Cai, W., and Shalaev,

V. M. The Ag dielectric function in plasmonic metamaterials. *Optics express*, **2008**

16(2), 1186-1195.

(69) Kittel, C. *Introduction to solid state physics.* John Wiley & sons, inc. **2005**

(70) Zhao, Y., Pan, H., Lou, Y., Qiu, X., Zhu, J., and Burda, C. Plasmonic Cu nanocrystals: optical and structural properties of copper-deficient copper (I) sulfides. *Journal of the American Chemical Society* **2009**, 131(12), 4253-4261.

(71) Comin, A., Manna, L. New materials for tunable plasmonic colloidal nanocrystals.

Chemical Society Reviews **2014**, 43(11), 3957-3975.

(72) Faucheaux, J. A., Stanton, A. L., and Jain, P. K. Plasmon resonances of semiconductor nanocrystals: physical principles and new opportunities. *The journal of physical chemistry letters* **2014**, 5(6), 976-985.

(73) Garcia, G., Buonsanti, R., Runnerstrom, E. L., Mendelsberg, R. J., Llordes, A., Anders, A., and Milliron, D. J. Dynamically modulating the surface plasmon resonance of doped semiconductor nanocrystals. *Nano letters* **2012**, 10, 4415-4420.

(74) Naik, G. V., Shalaev, V. M., Boltasseva, A. (2013). Alternative plasmonic materials: beyond gold and silver., *Advanced Materials* **2013**, 25(24), 3264-3294.

(75) Routzahn, A. L., White, S. L., Fong, L. K., Jain, P. K. Plasmonics with doped quantum dots. *Israel Journal of Chemistry* **2012**, 52(11-12), 983-991.

(76) Manthiram, K., Alivisatos, A. P. Tunable localized surface plasmon resonances in tungsten oxide nanocrystals. , *Journal of the American Chemical Society* **2012**, 134(9), 3995-3998.

(77) Huang, Q., Hu, S., Zhuang, J., Wang, X. MoO3–x-based hybrids with tunable localized surface plasmon resonances: chemical oxidation driving transformation from ultrathin nanosheets to nanotubes. *Chemistry-A European Journal* **2012**, 18(48), 15283-15287.

(78) Andualem, W. W. Green Synthesis of CuO Nanoparticles for the Application of dye Sentized Solar Cell **2020**.

(79) Saravanan, R.; Gracia, F.; Stephen, A. Basic principles, mechanism, and challenges of photocatalysis. *Nanocomposites for visible light-induced photocatalysis* **2017**, 19-40.

(80) Polarz, S., Strunk, J., Ischenko, V., Van den Berg, M. W., Hinrichsen, O., Muhler, M., and Driess, M. On the role of oxygen defects in the catalytic performance of zinc oxide. *Angewandte Chemie International Edition* **2006**, 45(18), 2965-2969.

(81) Thompson, T. L., and Yates, J. T. TiO2-based photocatalysis: surface defects, oxygen and charge transfer. *Topics in Catalysis*, **2005**, 35, 197-210.

(82) Nowotny, M. K., Sheppard, L. R., Bak, T., and Nowotny, J. Defect chemistry of titanium dioxide. Application of defect engineering in processing of TiO2-based photocatalysts. *The Journal of Physical Chemistry C*, **2008**, 112(14), 5275-5300.

(83) Li, X.; Yu, J.; Jaroniec, M. Hierarchical photocatalysts. *Chemical Society Reviews* **2016**, 45(9), 2603-2636.

(84) Wang, X.; Yu, J. C.; Ho, C.; Hou, Y.; Fu, X. Photocatalytic activity of a hierarchically macro/mesoporous titania. *Langmuir* **2005**, 21(6), 2552-2559.

(85) Kresge, A. C.; Leonowicz, M. E.; Roth, W. J.; Vartuli, J. C.; Beck, J. S. Ordered mesoporous molecular sieves synthesized by a liquid-crystal template mechanism. *Nature* **1992**, 359(6397), 710-712.

(86) Yu, J.; Jimmy, C. Y.; Zhang, L.; Wang, X.; Wu, L. Facile fabrication and characterization of hierarchically porous calcium carbonate microspheres. *Chemical communications* **2004**, (21), 2414-2415.

(87) McCoy, D. E.; Shneidman, A. V.; Davis, A. L.; Aizenberg, J. Finite-difference time-domain (FDTD) optical simulations: a primer for the life sciences and bio-inspired engineering. *Micron* **2021**, 151, 103160.

(88) Salunkhe, R. R.; Kaneti, Y. V.; Kim, J.; Kim, J. H.; Yamauchi, Y. Nanoarchitectures for metal–organic framework-derived nanoporous carbons toward supercapacitor applications. *Accounts of chemical research* **2016**, 49(12), 2796-2806.

(89) Sun, H.; Xu, Z.; Gao, C. Multifunctional, ultra-flyweight, synergistically assembled carbon aerogels. *Advanced materials* **2013**, 25(18), 2554-2560.

(90) Moreno-Castilla, C.; Maldonado-Hódar, F. J. Carbon aerogels for catalysis applications: An overview. *Carbon* **2005**, 43(3), 455-465.

(91) Coleman, J. N.; Khan, U.; Blau, W. J.; Gun'ko, Y. K. Small but strong: a review of the mechanical properties of carbon nanotube–polymer composites. *Carbon* **2006**, 44(9), 1624-1652.

(92) Ho, M. Y.; Khiew, P. S.; Isa, D.; Tan, T. K.; Chiu, W. S.; Chia, C. H. A review of metal oxide composite electrode materials for electrochemical capacitors. *Nano* **2014**, 9(06), 1430002.

(93) Yoo, H. D.; Han, S. D.; Bayliss, R. D.; Gewirth, A. A.; Genorio, B.; Rajput, N. N.; Cabana, J. Rocking-chair-type metal hybrid supercapacitors. *ACS applied materials & interfaces* **2016**, 8(45), 30853-30862.

(94) Trasatti, S.; Buzzanca, G. Ruthenium dioxide: A new interesting electrode material. Solid state structure and electrochemical behaviour. *Journal of electroanalytical chemistry and interfacial electrochemistry* **1971**, 29(2), A1-A5.

(95) Conway, B. E. Electrochemical supercapacitors: scientific fundamentals and technological applications. *Springer Science & Business Media* **2013** p.698.

(96) Subramani, K.; Sathish, M. Facile synthesis of ZnO nanoflowers/reduced graphene oxide nanocomposite using zinc hexacyanoferrate for supercapacitor applications. *Materials Letters* **2019**, 236, 424-427.

(97) Zhi, M.; Xiang, C.; Li, J.; Li, M.; Wu, N. Nanostructured carbon–metal oxide composite electrodes for supercapacitors: a review. *Nanoscale* **2013**, 5(1), 72-88.

(98) Simon, P.; Gogotsi, Y. Materials for electrochemical capacitors. *Nature materials* **2008**, 7(11), 845-854

(99) Conway, B. E.; Pell, W. G. Power limitations of supercapacitor operation associated with resistance and capacitance distribution in porous electrode devices. *Journal of power sources* **2002**, 105(2), 169-81.

(100) Raut, A. S.; Parker, C. B.; Glass, J. T. A method to obtain a Ragone plot for evaluation of carbon nanotube supercapacitor electrodes. *Journal of Materials Research* **2010**, 25, 1500-1506.

(101) Dubal, D. P.; Ayyad, O.; Ruiz, V.; Gomez-Romero, P. Hybrid energy storage: the merging of battery and supercapacitor chemistries. *Chemical Society Reviews* **2015**, 44(7), 1777-1790.

(102) Cericola, D.; Ruch, P. W.; Kötz, R.; Novák, P.; Wokaun, A. Simulation of a supercapacitor/Li-ion battery hybrid for pulsed applications. *Journal of Power Sources* **2020**, 195(9), 2731-2736.

(103) Reichbach, N.; Mellincovsky, M.; Peretz, M. M.; Kuperman, A. Long-term wide-temperature supercapacitor ragone plot based on manufacturer datasheet. *IEEE Transactions on Energy Conversion* **2015**, 31(1), 404-406.

(104) Elgrishi, N.; Rountree, K. J.; McCarthy, B. D.; Rountree, E. S.; Eisenhart, T. T.; Dempsey, J. L. A practical beginner's guide to cyclic voltammetry. *Journal of chemical education* **2018**, 95(2), 197-206.

(105) Wang, G.; Zhang, L.; Zhang, J. A review of electrode materials for electrochemical supercapacitors. *Chemical Society Reviews* **2012**, 41(2), 797-828.

(106) Lufrano, F.; Staiti, P. Performance improvement of Nafion based solid state electrochemical supercapacitor. *Electrochimica Acta* **2004**, 49(16), 2683-2689.

(107) Hulicova-Jurcakova, D.; Seredych, M.; Lu, G. Q.; Bandosz, T. J. Combined ef- fect of nitrogen-and oxygen-containing functional groups of microporous activated carbon on its electrochemical performance in supercapacitors. *Advanced functional materials* **2009**, 19(3), 438-447.

(108) Wang, G.; Fu, L.; Zhao, N.; Yang, L.; Wu, Y.; Wu, H. An aqueous rechargeable lithium battery with good cycling performance. *Angewandte Chemie International Edition* **2007**, 46(1-2), 295-297.

(109) Marom, R.; Amalraj, S. F.; Leifer, N.; Jacob, D.; Aurbach, D. A review of advanced and practical lithium battery materials. *Journal of Materials Chemistry* **2011**, 21(27), 9938-9954.

(110) Zhong, C.; Deng, Y.; Hu, W.; Qiao, J.; Zhang, L.; Zhang, J. A review of electrolyte materials and compositions for electrochemical supercapacitors. *Chemical Society Reviews* **2015**, 44(21), 7484-7539.

(111) Balducci, A.; Bardi, U.; Caporali, S.; Mastragostino, M.; Soavi, F. Ionic liquids for hybrid supercapacitors. *Electrochemistry communications* **2004**, 6(6), 566-570.

(112) Chen, Y.; Zhang, X.; Zhang, D.; Yu, P.; Ma, Y. High performance supercapacitors based on reduced graphene oxide in aqueous and ionic liquid electrolytes. *Carbon* **2011**, 49(2), 573-580.

(113) Meng, F.; Fang, Z.; Li, Z.; Xu, W.; Wang, M.; Liu, Y.; Guo, X. Porous Co_3O_4 materials prepared by solid-state thermolysis of a novel Co-MOF crystal and their superior energy storage performances for supercapacitors. *Journal of materials chemistry A* **2013**, 1(24), 7235-7241.

(114) Armand, M.; Endres, F., MacFarlane, D. R.; Ohno, H.; Scrosati, B. Ionic-liquid materials for the electrochemical challenges of the future. *Nature materials* **2009**, 8(8), 621-629.

(115) Galiński, M.; Lewandowski, A.; Stępniak, I. Ionic liquids as electrolytes. *Electrochimica acta* **2006**, 51(26), 5567-5580.

(116) Zhang, Y.; Feng, H.; Wu, X.; Wang, L.; Zhang, A.; Xia, T.; Zhang, L. Progress of electrochemical capacitor electrode materials: A review. *International journal of hydrogen energy* **2009**, 34(11), 4889-4899.

(117) Chuang, C. M.; Huang, C. W.; Teng, H.; Ting, J. M. Effects of carbon nanotube grafting on the performance of electric double layer capacitors. *Energy & Fuels* **2010**, 24(12), 6476-6482.

(118) Zhang, D.; Zhang, X.; Chen, Y.; Yu, P.; Wang, C.; Ma, Y. Enhanced capaci- tance and rate capability of graphene/polypyrrole composite as electrode material for supercapacitors. *Journal of Power Sources* **2011**, 196(14), 5990-5996.

(119) Hu, C. C.; Chang, K. H.; Lin, M. C.; Wu, Y. T. Design and tailoring of the nanotubular arrayed architecture of hydrous RuO_2 for next generation supercapacitors. *Nano letters* **2006**, 6(12), 2690-2695.

(120) Takaloo, S.; Zand, M. M. Wearable electrochemical flexible biosensors: With the focus on affinity biosensors. *Sensing and Bio-Sensing Research* **2021**, 32, 100403.

(121) Biesheuvel, P. M.; Dykstra, J. E. The difference between Faradaic and Nonfaradaic processes in Electrochemistry. *arXiv preprint arXiv* **2018**:1809.02930, 1-10.

(122) Guan, L.; Yu, L.; Chen, G. Z. Capacitive and non-capacitive faradaic charge storage. *Electrochimica Acta* **2016**, 206, 464-478.

(123) Avendano, E.; Berggren, L.; Niklasson, G. A.; Granqvist, C. G.; Azens, A. Electrochromic materials and devices: Brief survey and new data on optical absorption in tungsten oxide and nickel oxide films. *Thin solid films* **2006**, 496(1), 30-36.

(124) Lampert, C. M.; Granqvist, C. G. Large-area chromogenics: materials and devices for transmittance control. *In Society of Photo-Optical Instrumentation Engineers (SPIE)* **1990** Conference Series (Vol. 10304).

(125) Svensson, J.; Granqvist, C. G. Electrochromic tungsten oxide films for energy efficient windows. *Solar energy materials* **1984**, 11(1-2), 29-34.

(126) Granqvist, C. G. Solar energy materials. *Advanced Materials* **2003**, 15(21), 1789-1803.

(127) Cai, G.; Wang, J.; Lee, P. S. Next-generation multifunctional electrochromic devices. *Accounts of chemical research* **2006**, 49(8), 1469-1476.

(128) Jensen, J.; Hösel, M.; Kim, I.; Yu, J. S.; Jo, J.; Krebs, F. C. Fast switching ITO free electrochromic devices. *Advanced Functional Materials* **2014**, 24(9), 1228-1233.

(129) Yu, S.; Ma, X.; Li, X.; Li, J.; Gong, B.; Wang, X. Enhanced adhesion of Ag nanowire based transparent conducting electrodes for application in flexible electrochromic devices. *Optical Materials* **2021**, 120, 111414.

VITA

EDUCATION

2023, PhD in Photonics Science and Engineering, Graduate School of Engineering and Sciences, İzmir Institute of Technology, İzmir/Turkey
Thesis Title: Synthesis, Properties and Applications of Tungsten Oxide Nanostructures
Supervisor: Prof. Dr. Sinan Balcı

2019, M.Sc. in Photonics Science and Engineering, Graduate School of Engineering and Sciences, İzmir Institute of Technology, İzmir/Turkey
Thesis Title: Functionalization and thickness dependent properties of single layer dichalcogenides
Supervisor: Prof. Dr. Hasan Şahin

2017, B.Sc. in Astronomy and Space Sciences, Ege University